

## REVIEW

# Revisiting the classification of NIR-absorbing/emitting nanomaterials for *in vivo* bioapplications

Tzu-Ming Liu<sup>1,2</sup>, João Conde<sup>3,4</sup>, Tomasz Lipiński<sup>5,6</sup>, Artur Bednarkiewicz<sup>6,7</sup> and Chih-Chia Huang<sup>8</sup>

With the development of nonlinear optics and new imaging methods, near-infrared (NIR) light can excite contrast agents to probe biological specimens both functionally and structurally with a deeper imaging depth and a higher spatial resolution than linear optical approaches. There is considerable and growing interest in how biological specimens respond to NIR light. Moreover, the visible absorption band of most functional nanomaterials becomes NIR-excitible through multiphoton processes, thus allowing multifunctional imaging and combined therapy with noble metal and magnetic nanoparticles both *in vitro* and *in vivo*. A groundbreaking example is the use of different laser techniques to excite single-type NIR-absorbing/emitting nanomaterials to produce multiphoton emission by femtosecond lasers using either a remote control system for photodynamic therapy or photo-induced chemical bond dissociation. These techniques provided superior anatomical resolution and detection sensitivity for *in vivo* tumor-targeted imaging than those offered by conventional methods. Here we summarize the most recent progress in the development of smart NIR-absorbing/emitting nanomaterials for *in vivo* bioapplications.

NPG Asia Materials (2016) 8, e295; doi:10.1038/am.2016.106; published online 5 August 2016

## INTRODUCTION

With functionalized loading matrices, nanometer-sized drug carriers can cross physiological barriers, effectively deliver therapeutics to pathological foci and release their cargo ‘on-demand’ by photo-/chemo-/thermo-triggering.<sup>1</sup> On the one hand, functionalization prevents the aggregation and degradation of therapeutics when passing through various physiological environments. On the other hand, it allows the nanomedicines to circulate through the blood long enough to specifically target desired sites. Finally, it concentrates the dose of therapeutics on the target sites and reduces unwanted toxicity to organisms and healthy tissues. To visualize the pharmacokinetics of the nanomedicines on the molecular scale and to verify the targeting design, nanomedicines need to be labeled with contrast agents that are suitable for at least one visualization method (for example, optical, magnetic resonance imaging, radioisotope thermoelectric generator or photoacoustic). One of the most promising visualization techniques is optical imaging because of its capability of *in vivo* imaging, relatively high resolution, non-invasiveness, simple detection and high contrast. The distributions and dynamics of the nanomedicines can then be monitored by *in vivo* microscopy. However, turbid biological tissues

have strong Rayleigh and Mie scattering in the visible wavelength range. Pigments and blood hemoglobin also introduce strong absorption for wavelengths shorter than 1000 nm. Therefore, to observe deep tissue and to activate nanomedicines through optical excitations, these nanocarriers need to have near-infrared (NIR) absorption and emission properties to overcome the degradation of imaging quality and the attenuation of illumination intensities arising from tissue scattering and absorption. To satisfy these requirements, several chemical and physical properties need to be designed and incorporated into nanomedicines. First, the surface properties need to be engineered to avoid self-aggregation, reduce non-specific adsorption of opsonin proteins in blood plasma and escape recognition by the reticuloendothelial system (RES). One of the most common strategies used to maintain stability when circulating in blood plasma is to engraft a layer of polymer, such as poly(ethylene glycol) (PEG), onto the surface of the particles to build up steric repulsion against opsonin proteins,<sup>2</sup> although PEG-specific antibodies can subsequently form.<sup>3</sup> Second, many NIR-active nanomaterials may not have chemical affinity or loading capacity for the drugs. Different materials and nanostructures have been designed to confine drugs to the particles’

<sup>1</sup>Institute of Biomedical Engineering, National Taiwan University, Taipei, Taiwan; <sup>2</sup>Molecular Imaging Center, National Taiwan University, Taipei, Taiwan; <sup>3</sup>Massachusetts Institute of Technology, Institute for Medical Engineering and Science, Harvard-MIT Division for Health Sciences and Technology, Cambridge, MA, USA; <sup>4</sup>School of Engineering and Materials Science, Queen Mary University of London, London, UK; <sup>5</sup>Institute of Immunology and Experimental Therapy, Wrocław, Poland; <sup>6</sup>Wrocław Research Centre EIT+, Wrocław, Poland; <sup>7</sup>Institute of Low Temp and Structure Research, Wrocław, Poland and <sup>8</sup>Department of Photonics, Center for Micro/Nano Science and Technology, and Advanced Optoelectronic Technology Center, National Cheng Kung University, Taipei, Taiwan

Correspondence: Dr T-M Liu, Institute of Biomedical Engineering, National Taiwan University, No. 1, Sec. 4, Roosevelt Road, Taipei 10617, Taiwan.

E-mail: tmliu@ntu.edu.tw

or Dr J Conde, Massachusetts Institute of Technology, Institute for Medical Engineering and Science, Harvard-MIT Division for Health Sciences and Technology, 45 Carleton Street E25, Cambridge, MA 02139, USA.

E-mail: jdconde@mit.edu

or Dr C-C Huang, Department of Photonics, Center for Micro/Nano Science and Technology, and Advanced Optoelectronic Technology Center, National Cheng Kung University, No. 1, University Road, Tainan 701, Taiwan.

E-mail: c2huang@mail.ncku.edu.tw

Received 17 January 2016; revised 27 May 2016; accepted 8 June 2016

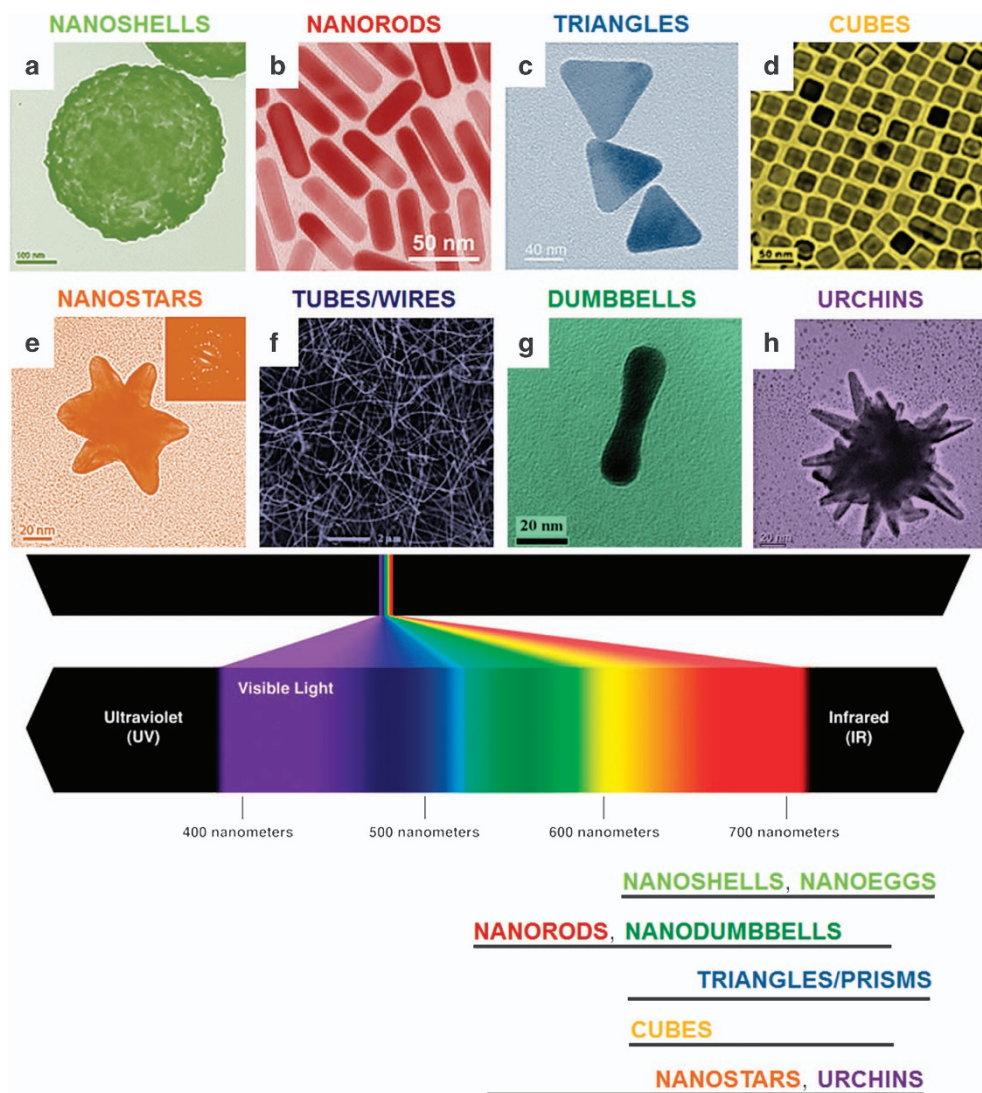


**Figure 1** The diversity on the NIR nanomaterial world. (a) nanoshells,<sup>9</sup> (b) nanorods,<sup>10</sup> (c) triangles/prisms,<sup>11</sup> (d) cubes and nanocages,<sup>8</sup> (e) nanostars,<sup>12</sup> (f) tubes and wires,<sup>13</sup> (g) dumbbells<sup>14</sup> and (h) urchins.<sup>15</sup>

inner or outer surfaces. Third, to avoid fast renal clearance from the circulation and non-specific permeation through fenestrated sinusoids of the liver/lymphoid/bone marrow/spleen, the carrier size must be  $> 20$  nm.<sup>4,5</sup> Although 100–200 nm-sized nanoparticles (NPs) may pass through the pores of vessels in the tumor microenvironment,<sup>6</sup> considering the tissue penetration and treatment outcome, particles  $< 50$  nm would be a better choice.<sup>7</sup> With these design considerations, an ideal drug carrier needs to possess the NIR-active properties, loading matrices, surface modifications and targeting functionalization, all within a size range of 20–50 nm.

To gain the NIR-active property, a diverse spectrum of anisotropic NIR nanomaterials have been reported in the literature, including nanorods, triangles/prisms, nanostars, cubes and nanocages, nanotubes, nanoshells and nanoeggs, nanourchins, nanocorns and nanodumbbells.<sup>8</sup> A pictorial representation of isotropic and anisotropic NIR nanomaterials is shown in Figure 1. Depending on the composition and physical nature of these contrast agents, NIR excitation and NIR emission becomes possible. For example, different shapes may shift the surface plasmon resonance (SPR) wavelengths toward NIR, create hotspots on the acute tips and be suitable for

different tumor microenvironments and physiological conditions. Another example includes Ag<sub>2</sub>S, whose emission band can be tuned in the NIR spectral range, which depends on the size of the quantum dots (QDs). Alternatively, neither the size nor the shape affects the spectral properties of lanthanide-doped nanomaterials, but the size significantly affects the emission quantum yield as well as circulation parameters.

#### FROM NIR-ABSORBING TO NIR-EMITTING NANOMATERIALS

Tissues are composed of many organic molecules that typically absorb (DNA, proteins, collagen, elastin, NADH and FAD) and sometimes emit (NADH, FAD, proteins and DNA) in the ultraviolet (UV)-visible region (Figure 2). Moreover, the scattering by heterogeneous tissue components is more efficient for shorter wavelengths, which significantly limits the penetration depth into thick tissue layers. Therefore, it is wise to shift both the excitation and emission wavelengths into the NIR region, which enables excitation deeper in the tissue and improves the optical/luminescence contrast. Nevertheless, such novel NIR labels require the nanomaterials to be engineered to efficiently absorb and emit in this spectral range. Inefficiency means higher

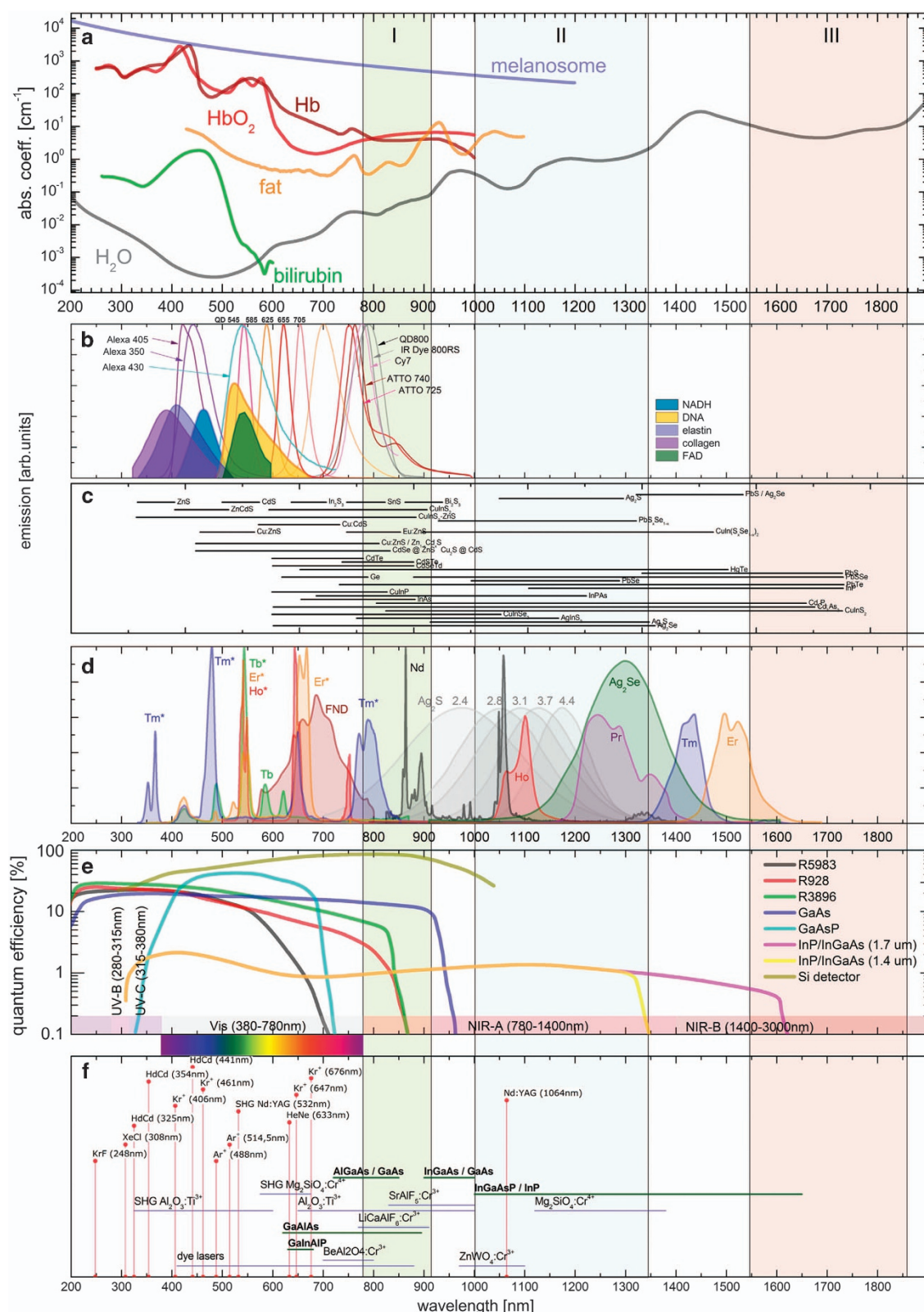


**Figure 2** Absorption coefficients of major tissue components (a), fluorescence spectra of major tissue components (NADH, DNA, elastin, collagen, FAD) combined with representative fluorescence spectra of commercial quantum dots and organic fluorophores (b), luminescence spectral range of semiconductors (c), (Stokes and anti-Stokes) luminescence spectra of lanthanide-doped nanoparticles, Ag<sub>2</sub>S and Ag<sub>2</sub>Se QDs (d), sensitivity of available photo-detectors (e) and available discrete (horizontal red lines) and tunable (vertical lines indicate tuning range) of state-of-the-art lasers (f).

excitation intensities, which can also be absorbed by the other ubiquitous building component of our bodies: water. Ultimately, this inefficiency may cause problems owing to overheating the illuminated tissue volume. Thus the optimal wavelength range is 700–940 nm, which is called the optical transmission window of the skin. This range varies depending on the tissue composition; however, tissue material is composed largely of water, which determines the best excitation/emission conditions for fluorescent labels and light-activated drug carriers in the NIR spectral region.

Although adipose tissues might contain less water, the baseline heating caused by absorption is inevitable. To avoid tissue damage owing to overheating, researchers have often employed pulsed lasers to achieve a sufficiently high instantaneous intensity of excitation while keeping the average power low.<sup>16</sup> The shorter the pulse width (that is, the duration) is, the less damage the heating will cause. For optical imaging, another challenge is to acquire detectable signals from nanomaterials. First, the materials need to be sensitized to infrared excitation and generate sufficient photons or acoustic energy. Second,

the generated signals need to overcome the scattering and attenuation of tissues to reach the detector of the imaging system. For the first criterion, the materials need to have a far-red or NIR absorption band. This property can be achieved by tailoring the SPR absorption band of metallic NPs by controlling the geometry or surface coating of the nanomaterials.<sup>17,18</sup> For the band-to-band transition, carbon-based nanomaterials have high absorption in the NIR region.<sup>19,20</sup> For solid-state materials doped with d-block and f-block elements, the NIR absorption (for  $\text{Yb}^{3+}$  at 980 nm or  $\text{Nd}^{3+}$  at ~800 nm) can provide a ladder-like upconversion (UC) route for visible luminescence (most typically, 470, 650 and 800 nm for  $\text{Tm}^{3+}$  and 520–540 and 650 nm for  $\text{Er}^{3+}$ ) or NIR (890/1060 nm for  $\text{Nd}^{3+}$ , 1470 nm for  $\text{Tm}^{3+}$ , 1310 nm for  $\text{Pr}^{3+}$ , 1185 nm for  $\text{Ho}^{3+}$  and 1525 nm for  $\text{Er}^{3+}$ ) at relatively low excitation intensity levels. For non-metallic materials that lack an infrared absorption band, noble metal surface coatings or ligands may extend the absorption to the NIR region.<sup>21</sup> Without NIR absorption, the only chance for effective signal generation relies on the nonlinear optical processes generated by picosecond or femtosecond

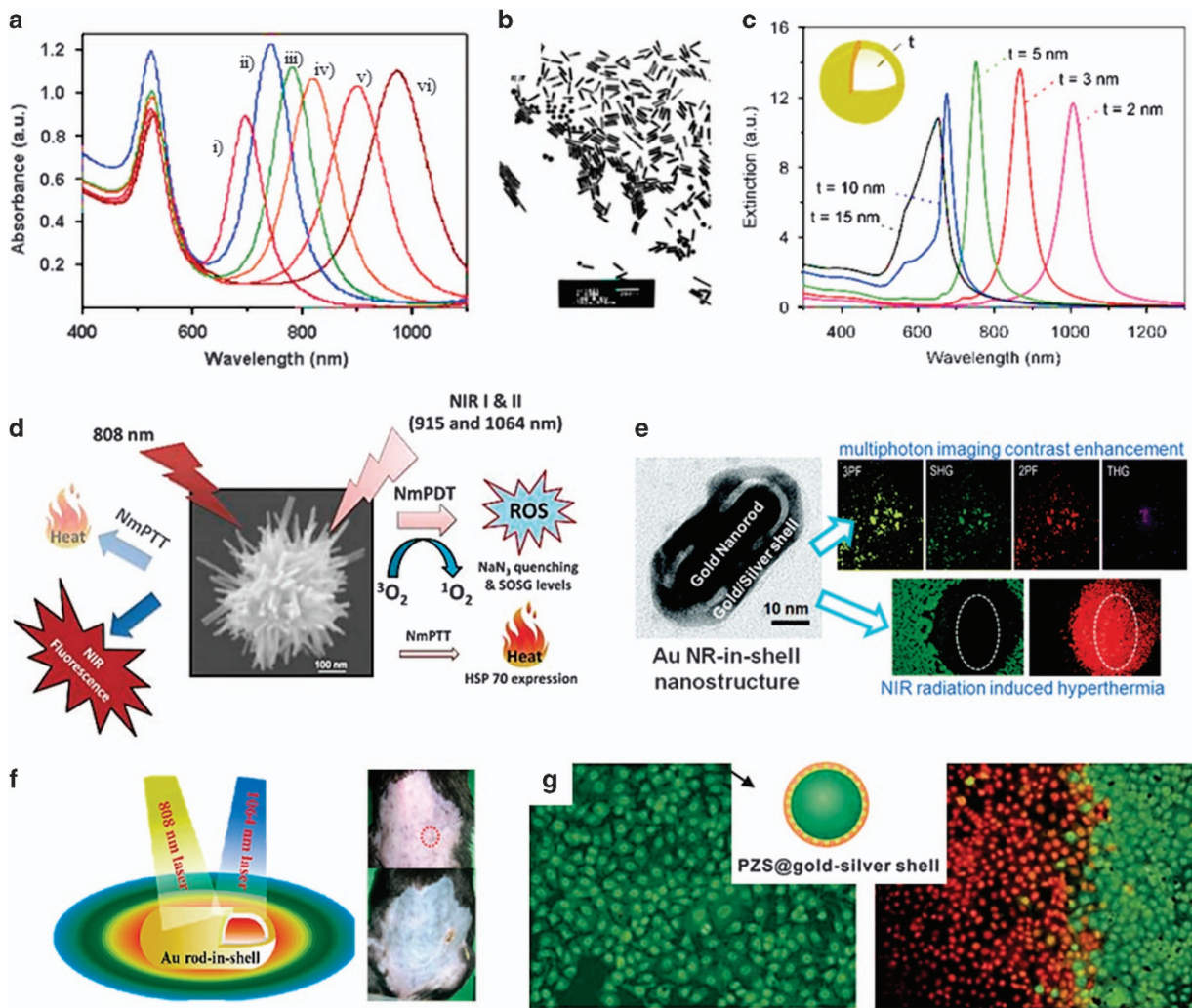


**Figure 3** (a) UV-visible absorption spectra of Au nanorods with different aspect ratios from (i) 2.2 to (vi) 4.7.<sup>26</sup> (b) A representative TEM image of the Au nanorod with  $L = 108 \pm 7 \text{ nm}$  and  $w = 22.8 \pm 1.6 \text{ nm}$  at an aspect ratio of 4.7.<sup>26</sup> (c) The extinction spectra of gold nanoshells (2–50 nm)-coated silica cores (60 nm) using DDA method.<sup>26</sup> (d) Schematic representation of the multibranched gold nanochinus for PTT at 808 nm and PDT at 915 and 1064 nm.<sup>32</sup> (e) Scheme illustrated the Au rod-in-shell nanostructures<sup>27</sup> and its corresponding TEM image shown in (e).<sup>17</sup> The nano-sample exhibited NIR hyperthermia of cancer cells *in vitro* (e) and *in vivo* (f). The red dotted circles in (f) indicate the location of the tumors. (g) Fluorescence images of HeLa cells (left) and HeLa cells (right) incubated with polymer core@Au/Ag shell nanostructures for 24 h and subjected to NIR irradiation for 15 min.<sup>9</sup>

lasers. The high instantaneous power of ultrafast lasers can excite nonlinear polarization for harmonic generation or multiphoton transition of electrons in nanomaterials. For the second excitation, infrared fluorescence or photoacoustic (PA) signals would be more appropriate. Semiconductor QDs with a high quantum yield can only emit in the 650–700 nm range. Semiconductor QDs can be two-photon excited by 1–1.2  $\mu\text{m}$  femtosecond lasers.<sup>22</sup> For longer wavelength fluorescence at 700–800 nm, nanomaterials need to be coated or loaded with cyanine dyes, such as Cy7 (775 nm),<sup>23</sup> dialkylcarbocyanines (780 nm) or indocyanine green (810–830 nm).<sup>24</sup> Multiphoton excitation on metallic NPs may result in broad bands and relatively weak luminescence extending into the NIR wavelength range.<sup>17</sup> Thus far, only  $\text{Ag}_2\text{S}$  and  $\text{Ag}_2\text{Se}$  QDs and carbon nanotubes (CNTs) can emit IR fluorescence with wavelengths of approximately 1–1.4  $\mu\text{m}$ .<sup>19,25</sup> Longer emission wavelengths will start to suffer from water absorption and may not be suitable for imaging applications. For PA contrast in soft tissues, scattering and attenuation will be less problematic for acoustic waves.

## NIR-ABSORBING NPS

### Au nanoparticles

Commonly, generating strong photo-to-thermal conversion is achieved using anisotropic Au (inert), Ag (toxic) and Cu (mildly toxic) NPs as efficient photoabsorbers based on the localized SPR. Among these NPs, Au is chemically inert and rarely decomposes, thus enabling several applications in biomedicine.<sup>26</sup> Various types of Au nanostructures (for example, nanocages, nanorods and nanoplates) and hybrids (core-shell nanostructures) (Figures 1 and 3) have been developed for photothermal and photodynamic therapies, which have been extensively reviewed elsewhere.<sup>27–30</sup> These therapies usually use NIR-I lasers (650–950 nm) to successfully treat different cancer types.

For imaging deep tissues, the desired absorption band would rely on the second biological window (NIR-II, 1000–1350 nm).<sup>31,32</sup> This property can be achieved by longitudinal SPR in elongated Au nanomaterials (Figures 3a and b). For example, the dual phototherapeutic property of multibranched Au nanoechinus was induced by exciting the NPs with a single continuous wave NIR-II laser without the need for a photosensitizer (PS) additive (Figure 3d).<sup>32</sup> This example was the first demonstration of noble metal NPs excited by NIR-II light that can sensitize the formation of singlet oxygen and exert photodynamic therapy (PDT) effects to induce cancer cell apoptosis. The wavelength-dependent quantum yield for the sensitization of singlet oxygen was 19% at 915 nm and 22% at 1064 nm. In another example, Yeh and co-workers synthesized an Au nanorod-in-shell structure (Figure 3e) with a strong SPR absorption band that covered the NIR-I and NIR-II regions (Figure 3f).<sup>31</sup>

These NPs achieved a photothermal therapeutic destruction of tumors with 1064 nm laser light at an intensity of  $3 \text{ W cm}^{-2}$ , which is far above the skin tolerance threshold value of  $\sim 420 \text{ mW cm}^{-2}$  at 1064 nm recommended by the American National Standards Institute for the safe use of lasers.<sup>33</sup> Moreover, any residual silver ions that are involved in the Au nanorod-in-shell structure might introduce uncertain risk with a long-term treatment or when particles accumulate in the human body. However, this NIR-II SPR absorption from gold nanorods may disappear owing to cold melting,<sup>34</sup> which should be taken into account when considering bioimaging applications using photomedicines in deep tissue.

### Pd nanoparticles

The SPR peaks of palladium nanostructures are in the UV region, and it is difficult to shift them to NIR wavelengths. One solution is to create an alloy form of Ag-Pd with a hollow structure for tuning the

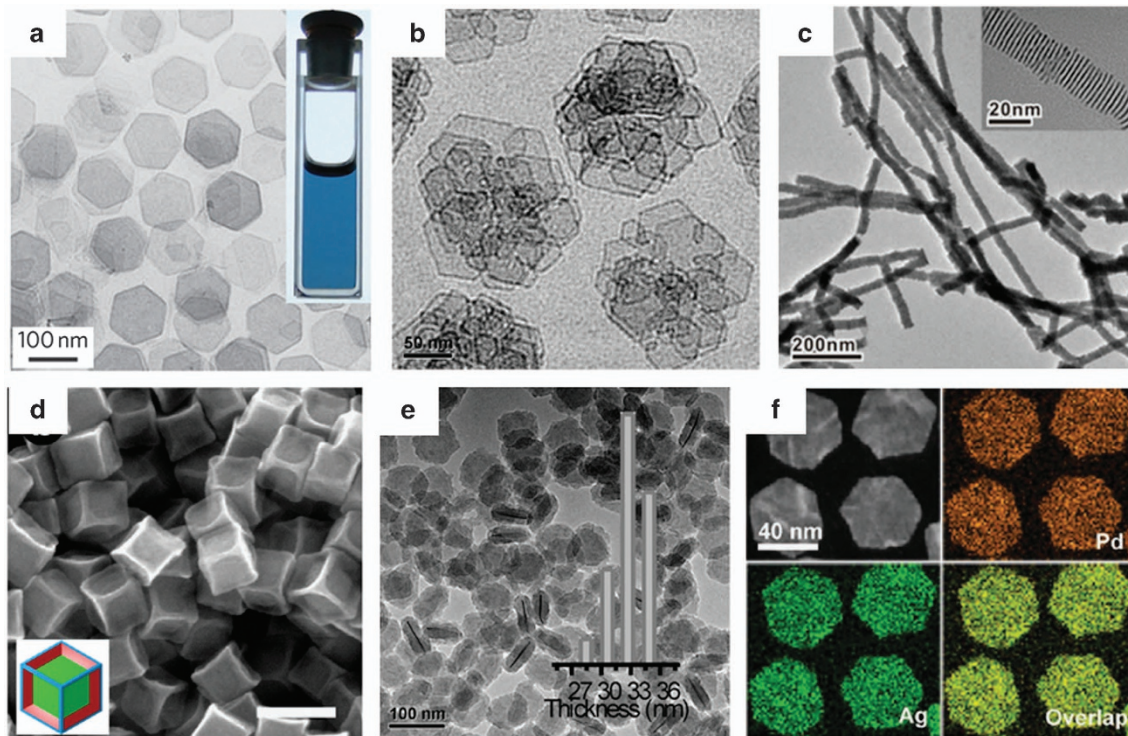


**Figure 4** TEM images of the (a) palladium nanosheets,<sup>37</sup> (b) corolla-like Pd mesocrystals,<sup>38</sup> (c) 1D Pd superlattice nanowires,<sup>39</sup> (d) Pd concave nanocubes,<sup>40</sup> (e) silica-coated Pd nanosheets.<sup>41</sup> (f) TEM and EDX mapping images of the Pd@Ag nanoplates.<sup>42</sup> Inset (a): photograph of an ethanol dispersion of the as-prepared palladium nanosheets.

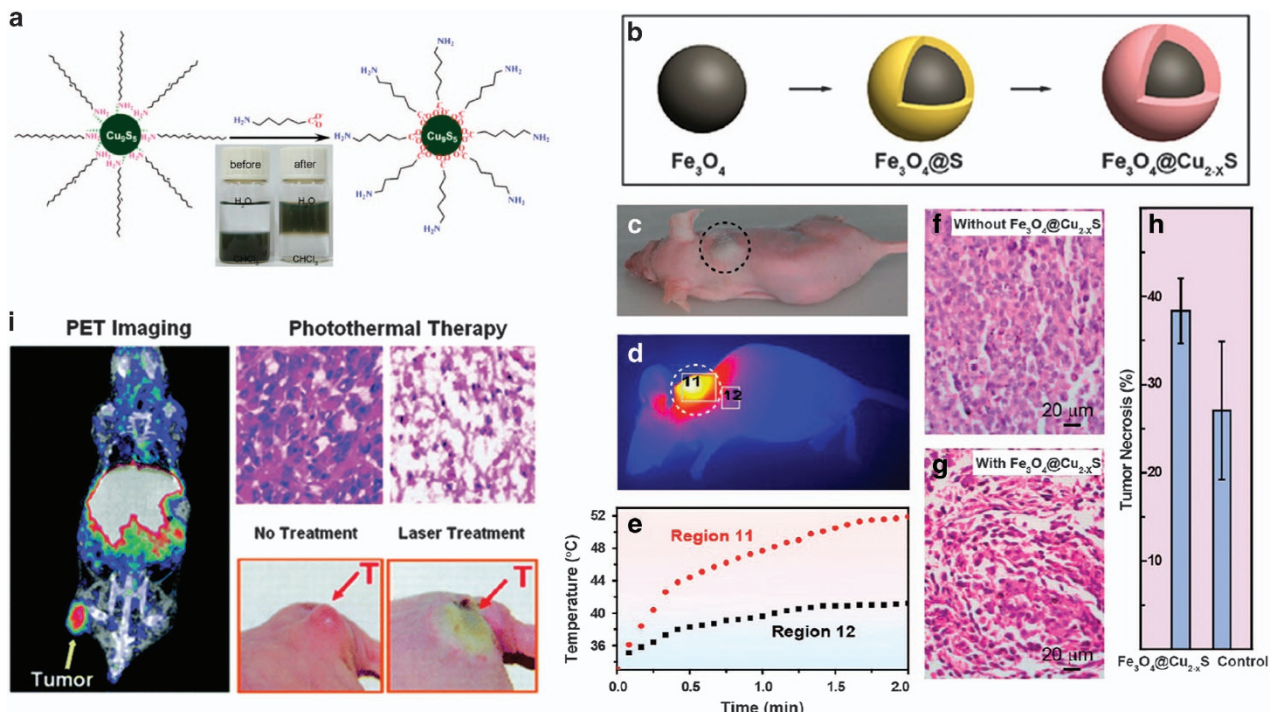


**Figure 5** (a) Schematic illustration of the preparation of the hydrophilic Cu<sub>9</sub>S<sub>5</sub> NCs via ligand exchange. Inset of the photo showing the Cu<sub>9</sub>S<sub>5</sub> NCs dispersed into different solvents (H<sub>2</sub>O and CHCl<sub>3</sub>) before and after the ligands' exchange.<sup>45</sup> (b) Experimental design for the synthesis of Fe<sub>3</sub>O<sub>4</sub>@Cu<sub>2-x</sub>S core-shell nanostructures. (c) Photograph of the tumor-bearing mouse (marked by a dashed circle). (d) Infrared thermal image of the tumor-bearing mouse treated with the Fe<sub>3</sub>O<sub>4</sub>@Cu<sub>2-x</sub>S nanoparticles after a 980 nm laser irradiation for 2 min. (e) Temperature profiles in regions 11 and 12 as a function of the irradiation time. (f, g) The representative hematoxylin and eosin-stained histological images of *ex vivo* tumor sections injected with: water only and an aqueous dispersion of polymer-modified Fe<sub>3</sub>O<sub>4</sub>@Cu<sub>2-x</sub>S nanoparticles (Cu content 50 p.p.m.), respectively. (h) Statistical analyses of necrosis in tumors treated with and without Fe<sub>3</sub>O<sub>4</sub>@Cu<sub>2-x</sub>S core-shell nanoparticles. The sections were irradiated with the 980 nm laser irradiation (0.6 W cm<sup>-2</sup>) for 10 min.<sup>47</sup> (i) Schematic illustration of the [<sup>64</sup>Cu]CuS NPs ideally suited for multifunctional molecular PET imaging and photothermal therapy.<sup>49</sup>

SPR bands from the UV-visible wavelength region to the NIR biological window.<sup>35</sup> However, having a silver component in the NP remains a concern for biocompatibility.<sup>36</sup>

Recently, Zheng and co-workers reported the synthesis of hexagonal Pd nanosheets (Figure 4a)<sup>37</sup> and Pd mesocrystals (Figure 4b)<sup>38</sup> with strong NIR absorbance, which are promising photothermal therapeutic agents for tumors and cancer cells. Forming Pd superlattice nanowires via the electrostatic self-assembly of thin-layer Pd nanosheets (Figure 4c)<sup>39</sup> and fabricating Pd concave nanocubes (Figure 4d)<sup>40</sup> provided a new strategy for altering the SPR bands toward long wavelengths. Indeed, the Pd nanosheets could be further hybridized with other inorganic nanomaterials (for example, silica (Figure 4e)<sup>41</sup> and silver (Figure 4f)).<sup>35,42</sup> Under NIR laser irradiation at 808 nm (>1 W of power density), the Pd, Pd@silica<sup>41</sup> and Pd (Ag@Pd) core-shell nanosheets<sup>42</sup> were capable of significant photo-to-thermal conversion with a concomitant destruction of the cancer cells. The different surface properties of Pd nanosheets modified the interaction between the NPs and cancer cells, thereby inducing a strong photothermal effect in *in vitro* studies.

Very recently, the same authors investigated the potential optical application of PA molecular imaging for *in vivo* cancer detection using Pd nanosheets.<sup>43</sup> Upon exposure to NIR laser light at 790 nm for 5 min (~4 mJ cm<sup>-2</sup>), poly(vinylpyrrolidone)-protected Pd nanosheets had superior photo-stability to that of traditional Au nanorods, which indicated that Pd nanosheets could be a good choice as a PA contrast agent for long-term observation. Furthermore, long-lasting PA imaging enhancement in SCC7 head and neck squamous cell

carcinoma was successfully performed in mice using PA tomography following systemic administration of Pd nanosheets (0.8 mg ml<sup>-1</sup>).

Nevertheless, most of the Pd-based nanosheets in development for photothermal therapy (PTT) are still limited to the cellular level and thus far have had no success in translation to preclinical and clinical trials.

#### Chalcogenide-based nanomaterials

Copper-chalcogenide-based materials (nanosize and microsize) are another class of inorganic agents that can be used for photomedicine. The d-d transition of electrons results in an absorption band over 900 nm. Hu and co-workers first reported the synthesis of microsized flower-like CuS particles (~1 μm).<sup>44</sup> Illumination with a 980 nm laser at 0.5 W cm<sup>-2</sup> intensity could excite hydrophilic CuS particles and convert thermal energy to ablate cancer cells. Other extraordinary photothermal agents for ablating tumors in mice include Cu<sub>9</sub>S<sub>5</sub> nanocrystals synthesized in the organic phase, followed by a ligand exchange process with 6-amino caproic acid (Figure 5a),<sup>45</sup> Cu<sub>2</sub>S<sub>4</sub> hollow structures<sup>46</sup> and Cu<sub>2-x</sub>S deposited on Fe<sub>3</sub>O<sub>4</sub> NPs (Figures 5b–h).<sup>47</sup> However, water molecules have an absorption band near 980 nm, which limits the practical application of CuS particles for safe *in vivo* photothermal treatment with a 980 nm laser. Recently, Li and co-workers investigated the use of a 1064 nm laser on CuS NPs, which avoids the water absorption band.<sup>48</sup> In this study, short laser pulses were required to evolve the PA tomography with CuS NPs. The contrast signal generation was up to ~5 cm deep by tracking the CuS NPs in agarose gel embedded in chicken breast muscle. Using a 1064 nm laser (ns pulsed model), <sup>64</sup>Cu-labeled PEG-CuS was

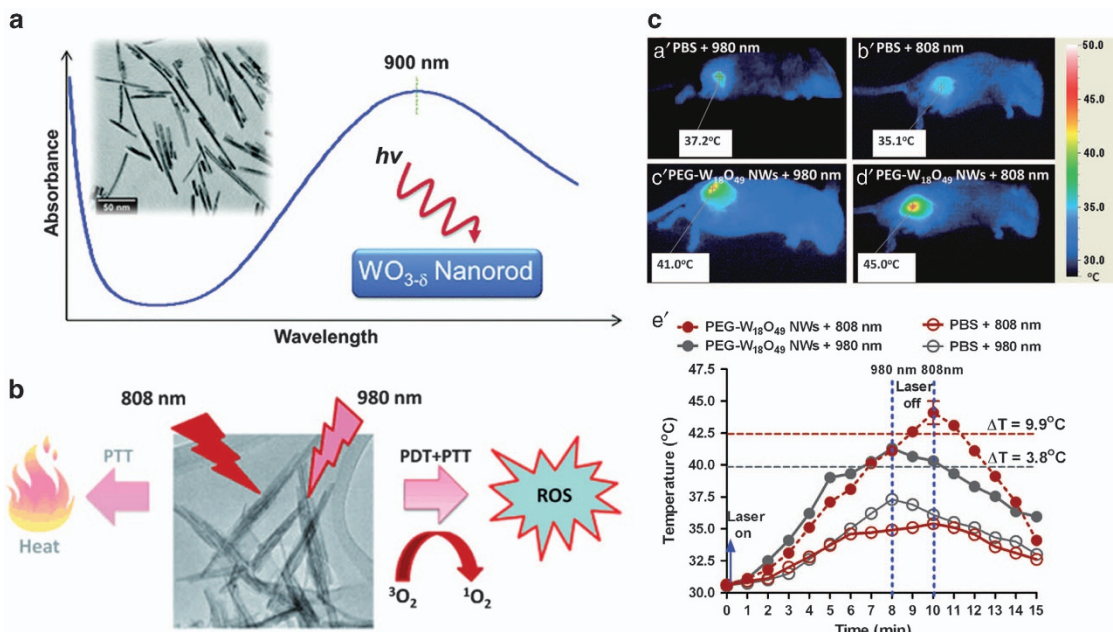


**Figure 6** (a) Photograph and absorption spectrum of WO<sub>2.83</sub> nanorods in *N*-methylpyrrolidone and TEM micrograph of WO<sub>2.83</sub> nanorods.<sup>56</sup> (b) Scheme illustrated PEGylated W<sub>18</sub>O<sub>49</sub> nanowires can generate PTT and ROS with 808 and 980 nm, respectively. (c) Photothermal images of mice under different conditions as labeled in the figures. (e') Temperature rise profiles as a function of irradiation time for conditions (a'–d'). Concentration of PEG-W<sub>18</sub>O<sub>49</sub> NWs injected into the tumor: 15 mg kg<sup>−1</sup>. The dashed blue lines are the time points where the lasers were turned off.<sup>57</sup>

successfully used to image the time-dependent accumulation of NPs in 4T1- and U87-tumor-bearing mice and to consequently monitor their therapeutic aptitude using PET (Figure 5i).<sup>49</sup>

Very recently, two-dimensional (2D) transition metal chalcogenides (FeS<sup>50</sup> and dichalcogenides (MoS<sub>2</sub><sup>51</sup> and WS<sub>2</sub><sup>52</sup>)) were developed as novel NIR-absorbing agents for PTT ablation for both *in vitro* and *in vivo* cancer PTT. Because their 2D layer structure is analogous to graphene, researchers have reported on the delivery of PSs<sup>51</sup> using the strong van der Waals force between aromatic molecules and the basal plane of the 2D metal sulfides. Specifically, this new PS-carried 2D transition metal chalcogenide makes them a promising nanoagent for combined PDT+PTT therapy.

For deeper PTT, Li *et al.*<sup>53</sup> reported a shape-controllable preparation of monodispersed CuTe (for example, nanocubes, nanoplates and nanorods), which displayed a significant absorption band at NIR-II wavelengths. The CuTe nanostructure was prepared using the thermal decomposition method. These CuTe NPs could enhance the photothermal ablation efficiency of cancer cells *in vitro*, and they were also investigated for their enhanced Raman signals for sensing molecules based on surface-enhanced Raman scattering.

#### Self-doped plasmonic NPs: wOx, indium tin oxide, and copper chalcogenide

Commonly, noble metal plasmonic materials present surface plasmons from the coherent delocalized electron oscillations at the interface between two media. Thus far, only inert Au NPs are ubiquitously used in photomedicine in various biological environments *in vitro* and *in vivo*. In addition to these major developments, the fabrication of non-metallic plasmonic NPs to tune the absorption bands of ultra-small NPs is a promising way to apply these particles in a broad range of wavelengths. Some fundamental limitations related to the physics of noble metals would be overcome by changing the free-carrier density of the semiconductor material<sup>54</sup> through carefully

designing the chemical synthesis technology to control heavily doped, nonstoichiometric ratios in the semiconductor NP composites. Although many extensive studies of the metallic behavior of heavily doped semiconductors in bulk materials and films were performed almost 40 years ago,<sup>55</sup> the development of ultra-small semiconductor NPs with controllable free-carrier densities for tuning their plasmonic absorption peak position is still in its infancy and remains a great challenge.

Recently, Manthiram and Alivisatos<sup>56</sup> demonstrated that WO<sub>3-δ</sub> nanorods exhibited a strong and tunable localized SPR (Figure 6a). The presence of a variety of oxygen-deficient stoichiometries in the WO<sub>3</sub> structure strongly affects the electrical and optical properties. When the δ value is greater than 0.1, the tungsten oxide undergoes an insulator-to-metal transition, and the conducting free electrons have NIR-I SPR absorption. This behavior could be explained according to the Mie-Gans theory. By heating the particles in air, the SPR absorption band was red shifted owing to the incorporation of oxygen ions in the WO<sub>3-δ</sub> structure, whereas charge carriers were annihilated after the additional dissolution of oxygen ions, which likely limited the strength of the SPR and its further application.

To date, numerous research groups have developed WO<sub>3-δ</sub> nanorods/nanowires as novel and effective candidates of NIR absorbents.<sup>57–60</sup> Chen *et al.*<sup>58</sup> and other groups reported the preparation of ultrathin PEGylated W<sub>18</sub>O<sub>49</sub> nanowires through a solvothermal reaction of a WCl<sub>6</sub> precursor in a mixture of PEG ( $M_w = 400$  Da) and ethanol solutions. A 980 nm wavelength laser was used to instantly convert photoenergy into thermal energy at a safe power density (0.72 W cm<sup>−2</sup>). However, a high dose (that is, up to 2000 p.p.m.) is necessary for the photothermal ablation of tumor tissues *in vivo*. Zhou *et al.*<sup>59</sup> further demonstrated that the PEG-coated tungsten oxide nanorods (with a length of 13.1 nm and diameter of 4.4 nm) used a 980 nm laser for PTT both *in vitro* and *in vivo*. The apoptosis of HeLa cells was subsequently induced. The cancerous cell viability rapidly

decreased with the increasing sample concentrations. Furthermore, similar to Au ( $Z=79$ ), metallic tungsten ( $Z=79$ ) can also serve as contrast agent in X-ray computed tomography (CT). Tungsten has an X-ray absorption coefficient ( $4.438 \text{ cm}^2 \text{ kg}^{-1}$  at 100 keV) higher than that of the clinical contrast iodine agent ( $1.94 \text{ cm}^2 \text{ kg}^{-1}$  at 100 keV). Consequently, the resultant PEG-coated tungsten oxide nanorods not only showed excellent capacity for photothermal ablation but they also provided superior tissue penetration depth and 3D renderings via monitoring *in vivo* X-ray transverse CT images of tumors.

To improve cancer diagnostics and therapy, Hu and co-workers utilized the HER-2 antibody to modify the surface of  $\text{W}_{18}\text{O}_{49}$  NPs for MM435 human breast cancer cells.<sup>60</sup> These NPs were prepared using a polyol method, producing very small particles of approximately 4.5 nm, smaller than the aforementioned tungsten oxide nanowires/nanorods. Importantly, a previous report established NPs with favorable accumulation in the lymph area for lymphatic imaging when the particle size was  $<10 \text{ nm}$ .<sup>61</sup> After systemic administration, HER-2 antibody-modified  $\text{W}_{18}\text{O}_{49}$  NPs can recognize lymph nodes in mice bearing HER-2-positive metastasis and can be clearly distinguished under CT guidance to selectively assist in the subsequent elimination after 1064 nm laser ablation.

Considering the possible overheating of water with laser irradiation at 980 nm, groups of Hu and co-workers and Zhu and co-workers developed new tungsten-oxide-based nanomaterials doped with  $\text{Na}^{+}$  and  $\text{Cs}^{+}$ .<sup>63</sup> This synthesis modification makes the NIR absorption of tungsten-oxide-based nanomaterials more resistant to oxidation. Compared with  $\text{Cs}_x\text{WO}_3$ <sup>63</sup> and  $\text{Rb}_{0.27}\text{WO}_3$ <sup>64</sup> NPs, the as-synthesized  $\text{Na}_{0.3}\text{WO}_3$  nanomaterials have an advantage as NIR photoabsorbers because of the superior photo-thermal efficacy and the potentially lower dose for administration *in vivo*. Surprisingly, Hwang and co-workers demonstrated the dual-modularity therapeutic effects of the combination of PTT and PDT after exposing PEGylated  $\text{W}_{18}\text{O}_{49}$  nanowires to a 980 nm laser irradiation treatment (Figures 6b and c).<sup>57</sup> These nanowires exhibited a strong fluorescence owing to the generation of singlet oxygen species. These results directly validated both the extra phototoxicity and the photothermal conversion for selectively injuring tumor tissue by treating

PEGylated  $\text{W}_{18}\text{O}_{49}$  nanowires and exciting them at 980 nm. However, the detailed mechanism for the creation of the electronic states of  $\text{W}_{18}\text{O}_{49}$  nanowires to produce singlet oxygen species remains unclear and requires further study.

### Fe<sub>3</sub>O<sub>4</sub> nanostructures

The development of new magnetic ( $\text{Fe}_2\text{O}_3$  and  $\text{Fe}_3\text{O}_4$ ) nanostructures and properties has received substantial attention owing to their potential applications in disease diagnostics and hyperthermia.<sup>65</sup> Compared with other reported hybrid nanostructures, the demonstrated optical properties of  $\text{Fe}_3\text{O}_4$  NPs provide new avenues of exploration in photomedicine, including phototherapy and optical imaging.

$\text{Fe}_2\text{O}_3$  particles have a good photocatalytic property owing to their flat band potential of 0.32 V vs normal hydrogen electrode (pH 0) and a band gap of 2.2 eV.<sup>66</sup> In fact, Wei *et al.*<sup>67</sup> reported that the junction formation in the  $\text{Fe}_3\text{O}_4@\text{Fe}_2\text{O}_3$  NPs produced a high level of photogenerated electrons, which could cross the interfacial junction and then transfer to the  $\text{Fe}_3\text{O}_4$  core. The authors observed efficient photo-decomposition of methylene blue dye in solution under visible-light irradiation ( $\lambda > 420 \text{ nm}$ ) owing to the specific interface photoelectric process. Thus a greater understanding of the electronic band structure of  $\text{Fe}_2\text{O}_3$  and  $\text{Fe}_3\text{O}_4$  materials<sup>68,69</sup> promoted the use of colloidal Fe-based oxide luminescence in early cancer optical diagnostics.

Meanwhile Fe(II) and Fe(III) in the octahedral sites of the inverse spinel-structured magnetite ( $\text{Fe}_3\text{O}_4$ ) material resulted in transition states in the NIR-II region based on an intervalence charge transfer.<sup>68</sup> Highly crystalline and highly pure magnetite has a promising transition property. Indeed, Sun and co-workers reported fabricating highly crystalline iron oxide NPs (24 nm) *via* thermal decomposition, which were then coated with a polysiloxane-containing copolymer for effective photothermal ablation.<sup>70</sup> The authors also evaluated the highly crystalline iron oxide NPs combined with an 885 nm laser at a power of  $>1 \text{ W cm}^{-2}$  in an *in vitro* system and in SUM-159 tumor-bearing mice. Despite these successful results, most reported synthesized  $\text{Fe}_3\text{O}_4$  NPs possess a nonstoichiometric structure and do

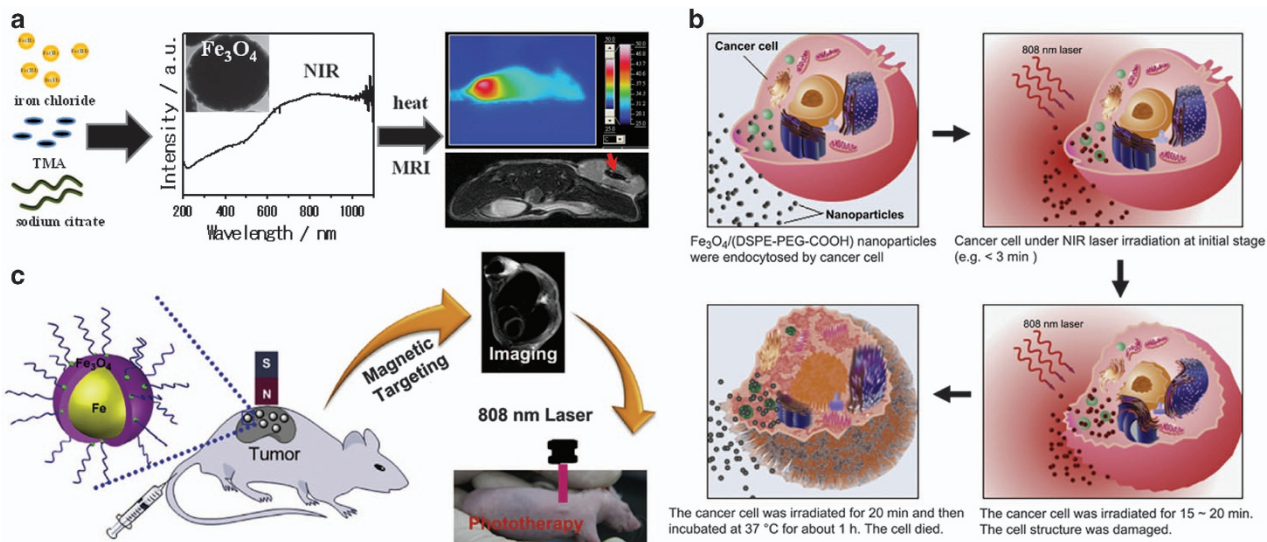


**Figure 7** (a) The preparation of NIR-activated  $\text{Fe}_3\text{O}_4$  nanostructures that can directly upgrade the iron oxide with MR contrast ability to be a MRI/photothermal theranostic agent.<sup>72</sup> (b) Schematic illustration of magnetic  $\text{Fe}@\text{Fe}_3\text{O}_4$  NPs targeting MRI and NIR photothermal therapy.<sup>73</sup> (c) Schematic illustration of  $\text{Fe}_3\text{O}_4$  nanoparticles coated with carboxyl-terminated poly(ethylene glycol)-phospholipid killing a cancer cell upon NIR laser irradiation.<sup>75</sup>

not have increased optical absorption bands in the NIR wavelength regions.<sup>71</sup> Interestingly, we recently found that coating the surface with molecules could broaden the absorption band (up to NIR wavelengths) of Fe<sub>3</sub>O<sub>4</sub> particles (13 and 440 nm in diameter) for effective PTT, novel two-photon fluorescence (TPF) imaging and magnetic resonance imaging (MRI) enhancement.<sup>21,72</sup>

Another approach was proposed to enhance the absorption by improving d-d transitions in the surface Fe<sup>3+/2+</sup> ions of Fe<sub>3</sub>O<sub>4</sub> NPs. In 2012, Liao and co-workers developed a trimesic acid/citrate-assisted hydrothermal reaction to fabricate sub-micron Fe<sub>3</sub>O<sub>4</sub> nanostructures with the NIR absorption band (Figure 7a).<sup>72</sup> When applying 808 nm laser light to excite the NIR particles, local heat could be generated to photo-ablate tumor cells both *in vitro* and *in vivo*. The image-guided approach is also applicable for clinical MR scanners owing to the superparamagnetic behavior of the as-synthesized NIR-Fe<sub>3</sub>O<sub>4</sub> particles. The photothermal effects of the magnetic Fe<sub>3</sub>O<sub>4</sub> NPs on cell and tumor tissue structures of esophageal cancer were further investigated (Figure 7b).<sup>73</sup> The surface of Fe<sub>3</sub>O<sub>4</sub> NPs modified with carboxy-terminated PEG-phospholipids enhanced their uptake by esophageal cancer cells and efficiently damaged the cellular organelles and inhibited esophageal tumor growth in mice. In addition to the surface reaction for improving the dispersion, different modifications of polymer<sup>74</sup> and inorganic<sup>47</sup> absorbers have been developed and have contributed to the strong absorbance in the NIR wavelengths. These polydopamine-functionalized Fe<sub>3</sub>O<sub>4</sub> NPs provided complementary imaging methods for PA imaging with MRI.<sup>74</sup> Currently, new PEGylated Fe@Fe<sub>3</sub>O<sub>4</sub> NP structures have shown strong photothermal conversion efficiency (~20%) (Figure 7c).<sup>75</sup> The presence of a metallic Fe core could increase the magnetization for magnetic targeting applications and the transverse relaxivity, which could lead to the development of combined photomedicine and theranostics with Fe<sub>3</sub>O<sub>4</sub>-based nanoreagents.

Extensive efforts have been devoted to the development of NP-mediated photothermal cancer therapy in the second NIR window, in which scattering losses are diminished and penetration is deeper. Very recently, Huang and co-workers reported Fe<sub>3</sub>O<sub>4</sub> cluster-structured NPs (CNP)s exhibiting a U-shaped absorption band with a low absorbance in the range of 750–950 nm and a progressive evolution in the second NIR region. These Fe<sub>3</sub>O<sub>4</sub> CNPs exhibited interesting NIR photonics for magnetomotive optical coherence tomography cellular imaging at 860 nm (~10 mW) combined with enhanced PTT using Fe<sub>3</sub>O<sub>4</sub> CNPs and a magnetic field at 1064 nm (380 mW cm<sup>-2</sup>).<sup>76</sup>

### Polymer NPs

Recently, a wide range of optical polymer materials has been developed to enable the self-assembly of NPs and optical-functional nanoshells for photothermal ablation of cancer cells *in vitro* and *in vivo*. For example, 20–60 nm NIR-optical polypyrrole (PPy) NPs were first developed by polymerizing a pyrrole monomer through a microemulsion system method in the aqueous phase using Fe(III) ions as the catalyst.<sup>77</sup> According to Zheng and co-workers, 50 nm PPy NPs possess a strong absorption band at ~850 nm, with a high extinction coefficient of  $2.38 \times 10^{10} \text{ M}^{-1} \text{ cm}^{-1}$ , and a significant photothermal conversion efficiency of 44.7%.<sup>78</sup> Biocompatible PPy NPs presented stable behavior in serum and have no apparent tissue toxicity *in vivo*. Because of their strong NIR absorption spectrum and biocompatibility, many groups have worked to demonstrate potential applications of sub-100 nm PPy NPs acting as photothermal agents that possess high photothermal conversion efficiency for tumor ablation.<sup>79</sup> Several strategies that integrate magnetic NPs and air

bubbles into PPy NPs have enabled additional medicinal functions in MRI<sup>80</sup> and ultrasound imaging,<sup>81</sup> respectively. These methods upgrade photothermal PPy nanocomposites to theranostic agents and enable the accumulation of concentrations in diseased areas sufficient to be visualized for both imaging and therapy purposes. In contrast to the MRI and ultrasound results, the intrinsic NIR absorption band of the PPy NPs enabled their use as a powerful biophotonics platform using the optical imaging modalities of optical coherence tomography<sup>82</sup> and PA technology<sup>83</sup> for tumor imaging. By exploiting NIR laser light and PPy optical contrast agents, a tissue treatment depth of ~4.3 cm was achieved.

## NIR-EMITTING NPs

### Nanohybrids

Integrating different materials into a single nano-entity can upgrade the nanomedical agents to promising multimodal agents for image-guided photothermal and photodynamic therapies. Molecular imaging with Au, I, ultra-small superparamagnetic iron oxides, Gd complexes and metal radionuclide elements (for example, <sup>64</sup>Cu, <sup>99m</sup>Tc, and <sup>111</sup>In) are examples of the different contrast agents that have been used to facilitate new clinical capabilities with CT, MRI and PET. However, most of these hybrid-based nanocomposites still have some drawbacks because of the different instruments that must be combined and the difficulty of real-time monitoring and detection *in situ*. Indeed, less strict requirements are imposed by integrating optical imaging and phototherapy together with a continuous-wave laser. In addition, sample preparation for multifunctional nanoagents has proven to be highly complex because of the multistep assembly of the desired components. The binding of NIR-based gold and MRI-functional iron oxide has been the most popular nanocomposite used in MRI-guided PTT.<sup>84</sup> Li et al.<sup>85</sup> reported a novel integration of Gd and <sup>64</sup>Cu ions with organic dyes, which led to an all-in-one nanoporphyrin platform for accessing NIR fluorescence imaging, MRI, PET, PTT and PDT (Figure 8). This versatile nanoporphyrin exhibits the comprehensive involvement of clinically relevant functions.

### Diamond NPs

More than 100 types of luminescence defects on diamonds have been reported thus far.<sup>86</sup> Among them, the nitrogen vacancy (N-V) defects have drawn considerable attention owing to its non-bleachable red (~700 nm) fluorescence with high quantum yields.<sup>87</sup> This defect consists of a substitutional nitrogen atom with an adjacent carbon vacancy. This N-V color center can be synthesized in type 1b synthetic diamond through electron irradiation (2 MeV) and subsequent annealing.<sup>87</sup> Recently, mass production of 20–30 nm fluorescence nanodiamonds (FNDs) has been realized.<sup>88</sup> Functionalized FNDs have been used for flow cytometry,<sup>89</sup> *in vivo* microscopy (Figure 9),<sup>90</sup> cancer cell imaging<sup>89</sup> and the long-term tracking of lung stem cells.<sup>91</sup> FND labeling does not affect the reproductive potential of organisms<sup>90</sup> or the regenerative functions of lung stem cells.<sup>91</sup> In addition to red fluorescence, green 531 nm fluorescence of N-V-N defects in type 1a diamond and blue 450 nm fluorescence in 5 nm nanodiamond-octadecylamine<sup>92</sup> have been developed for multiple color labeling.

Exploiting the relatively long fluorescence lifetime ( $\tau = 11.6 \text{ ns}$ ), FND labeling can remove the interference from tissue autofluorescence<sup>89,93</sup> with a time-delayed time-gated approach, which guarantees higher specificity in optical molecular imaging. The long fluorescence lifetime and high absorption cross-section also indicate a small saturation intensity of fluorescence, which is advantageous for achieving a small point-spread function in high-resolution

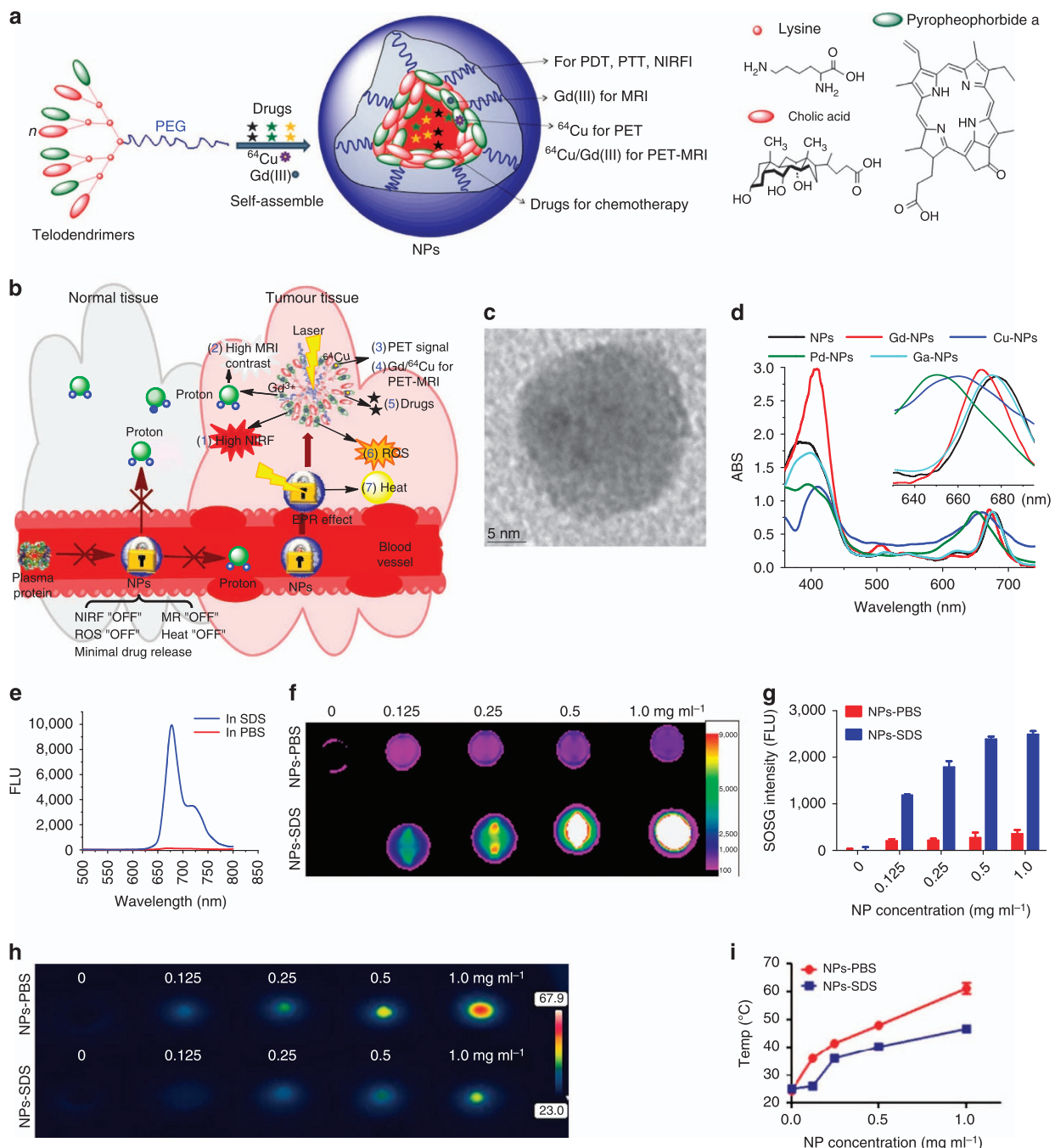


**Figure 8** (a) Schematic illustration of a multifunctional NP self-assembled by a representative porphyrin-telodendrimer,  $\text{PEG}^{5k}\text{-Por}_4\text{-CA}_4$ , composed of four pyropheophorbide-a molecules and four cholic acids attached to the terminal end of a linear PEG chain. (b) Schematic illustration of NPs as a smart 'all-in-one' nanomedicine platform against cancers. (c) TEM image of NPs (stained with phosphotungstic acid, PTA). (d) The absorbance spectra of NPs before and after chelating different metal ions. (e) Fluorescence emission spectra of NPs in the presence of PBS (red) and SDS (blue). Excitation: 405 nm. (f) Near-infrared fluorescence imaging of NP solution ( $10 \mu\text{l}$ ) in the absence and presence of SDS with an excitation bandpass filter at 625/20 nm and an emission filter at 700/35 nm. (g) Single oxygen generation of NPs in PBS and SDS upon light irradiation ( $690 \text{ nm at } 0.25 \text{ W cm}^{-2}$  for 60 s) measured by using SOSG as an indicator ( $n=3$ ). The results are expressed as mean  $\pm$  s.d. Concentration-dependent photothermal transduction of NPs: (h) thermal images and (i) quantitative temperature change curve ( $n=2$ ). The results are expressed as mean  $\pm$  s.d. The temperature of NP solution ( $10 \mu\text{l}$ ) in the absence and presence of SDS was monitored by a thermal camera after irradiation with NIR laser ( $690 \text{ nm}$ ) at  $1.25 \text{ W cm}^{-2}$  for 20 s.<sup>85</sup>

microscopies. Another interesting feature of nanodiamond fluorescence is the nature of the triplet transition in N-V defects. In a magnetic field, these degenerated levels will split owing to the Zeeman effect, and the magnetic resonance can thus be sensed through the optical fluorescence.

#### NIR-II carbon nanotubes

Single-walled CNTs (SWNTs) have been extensively studied as extraordinary NIR-I and NIR-II absorbers in photomedicine.<sup>94</sup> In fact, Harhaji-Trajkovic and co-workers extensively compared the photothermal activities of graphene nanosheets and CNTs.<sup>95</sup> Upon

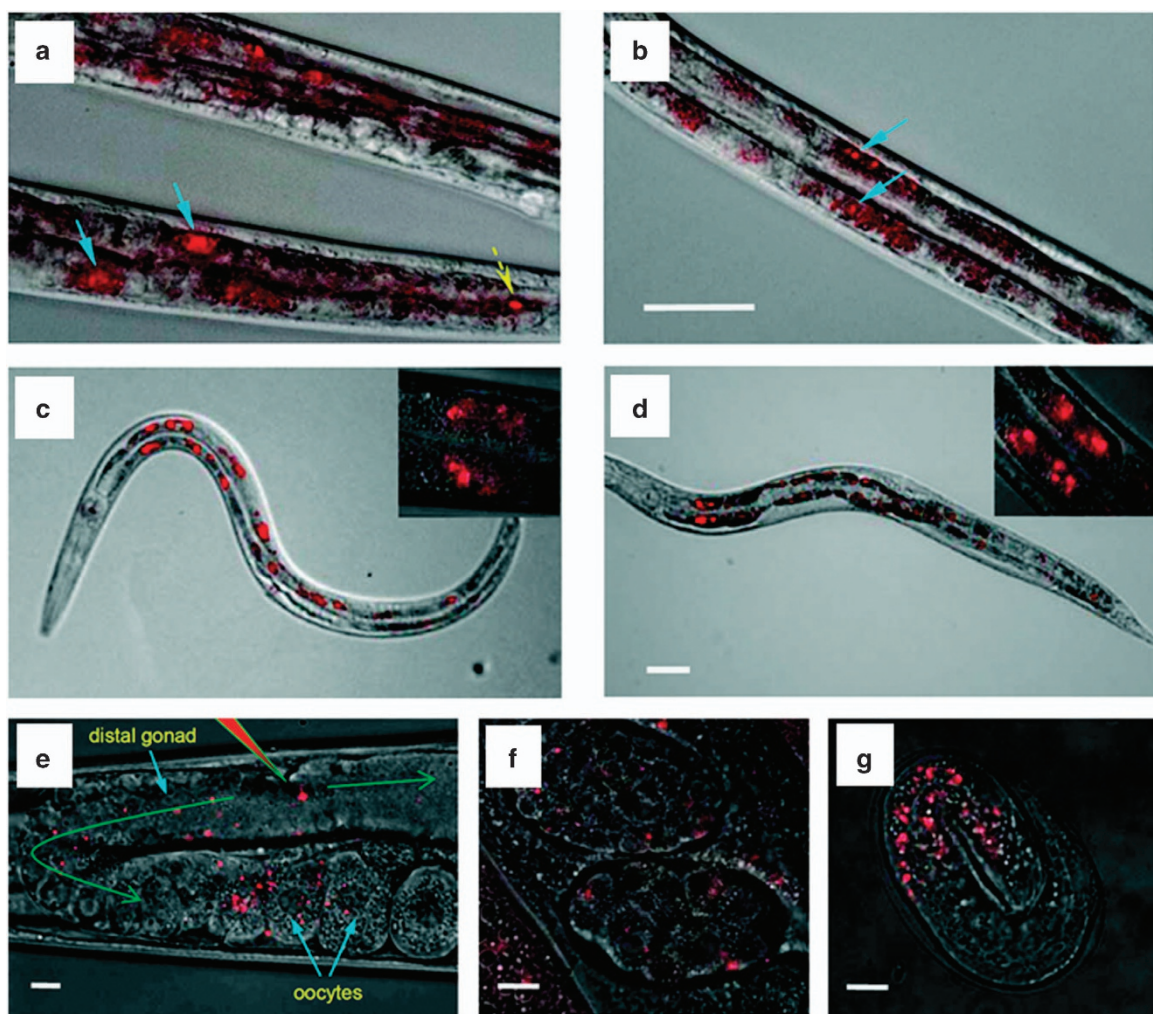


**Figure 9** Epifluorescence/DIC-merged images of wild-type *C. elegans* fed with bioconjugated FNDs. (a, b) Worms fed with dextran-coated FNDs (a) and BSA-coated FNDs (b) for 3 h. FNDs can be seen to be localized within the intestinal cells (blue solid arrows) and a few stay in the lumen (yellow dash arrow). (c and d) Worms fed with dextran-coated (c) and BSA-coated (d) FNDs for 3 h and recovered on to *E. coli* bacterial lawns for 1 h. In both cases, the FNDs staying in the lumen are excreted out, whereas the ones localized in the cells are retained. Insets:  $\times 100$  magnified images of the FNDs within the intestinal cells. Anterior is left and dorsal is up in all the figures. Scale bars are 50  $\mu\text{m}$ . (e–g) Epifluorescence/DIC-merged images of an injected worm (e) and its progeny at the early (f) and late (g) embryonic stages. The FNDs dispersed in the distal gonad and oocytes at approximately 30 min after injection (e). Green arrows indicate bulk streaming of FNDs with cytoplasmic materials and the red triangle indicates the site of injection. Note that the injected FNDs are present in the cytoplasm of many cells in the early embryos (f) but predominantly in the intestinal cells of the late embryo (g). Scale bars are 10  $\mu\text{m}$ . Reproduced and adapted with permission.<sup>90</sup> Copyright 2015, American Chemical Society.

exposure of a sample solution to 808 nm at 2 W cm<sup>-2</sup>, a suspension of poly-vinylpyrrolidone-coated graphene nanosheets emitted more heat than DNA- and sodium dodecyl sulfate-protected SWNTs. This difference was attributed to the poorer dispersivity observed in the bundle of nanotubes. The final concern is the difficulty in tailoring the tube dimensions of SWNTs, especially the length, through either the chemical etching reaction or mechanical destruction. This difficulty limits the flexibility of the geometric design for optimizing the biodistribution *in vivo*. New methods and platforms to address these issues are needed to promote practical clinical applications.

Another well-studied example of NIR CNTs is DNA-encased multiwalled CNTs. Gosh *et al.*<sup>96</sup> reported the use of DNA-encased multiwalled CNTs coupled with a 1064 nm CW laser at 2.5 W cm<sup>-2</sup> as a good solution to achieving the complete photothermal ablation of PC3 xenograft tumors in nude mice. Although this system did not affect normal tissues and displayed low toxicity over long-term

treatment, the acquired sample dose and laser power density remained too high for easy translation to clinical trials.

Except for therapeutic applications, the NIR-II fluorescence properties make CNTs a promising biophotonics platform for anatomical imaging and disease diagnostics, including the pharmacokinetic and optical imaging of tumor vessels as well as histopathology observations.<sup>97,98</sup> Strano and co-workers reported that SWNTs wrapped in 3,4-diaminophenylfunctionalized dextran were capable of real time and spatially resolved detection of nitric oxide production (Figure 10).<sup>99,100</sup> Indeed, several research groups have established the potential application of optical sensors based on CNTs for the *in vivo* detection of nitric oxide in mice<sup>99</sup> and in *Arabidopsis thaliana*.<sup>100,101</sup>

#### NIR carbon-based QDs

Numerous research groups have focused on surface engineering carbon and graphene QDs to investigate the fluorescence of

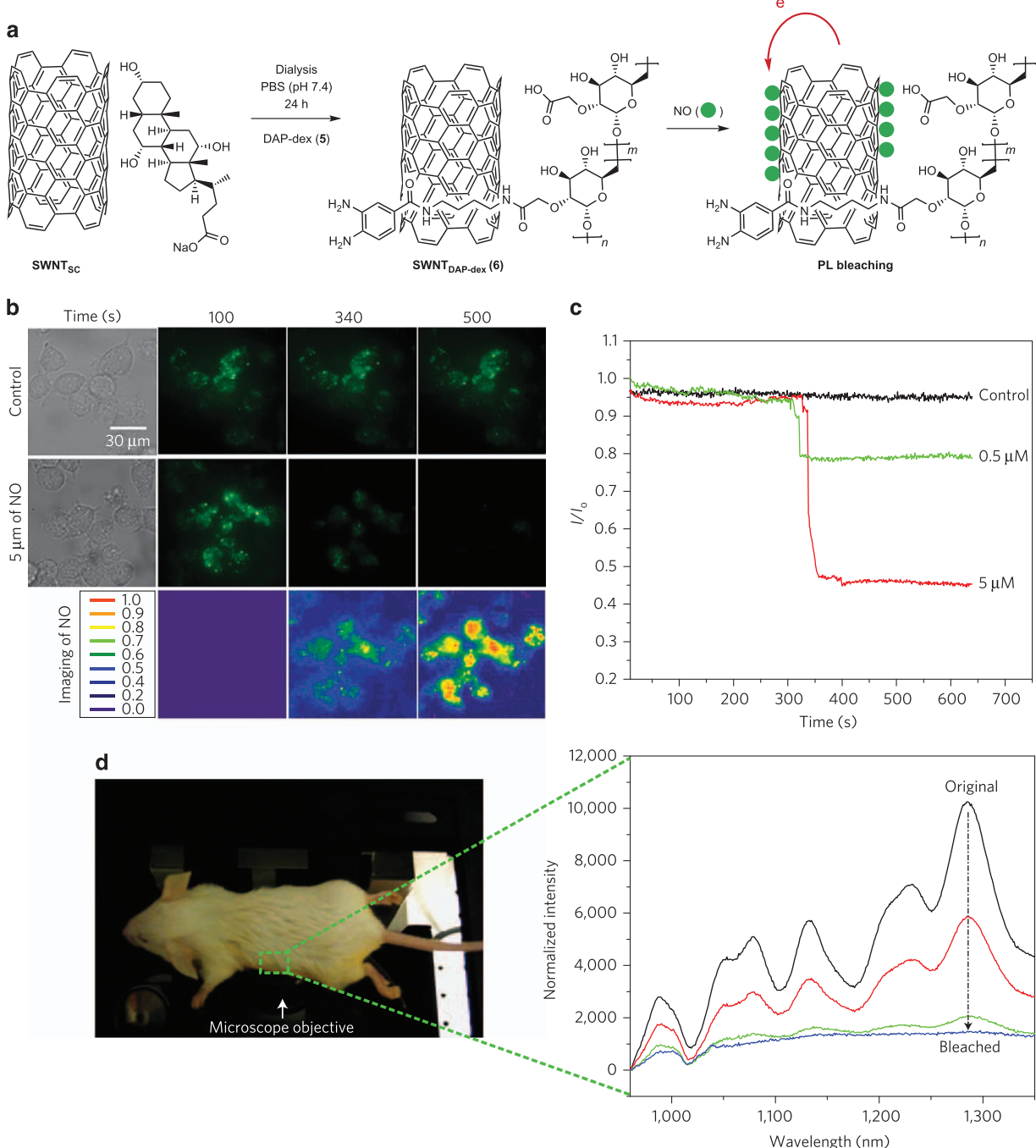


**Figure 10** (a) Synthesis of DAP-dex and preparation of SWNT DAP-dex by dialysis, and mechanism for NIR fluorescence bleaching by NO. PL, photoluminescence. (b) NIR fluorescence images and direct NO mappings of Raw 264.7 cells incorporating SWNT DAP-dex ( $1 \mu\text{g ml}^{-1}$ ) before and after NO addition. For the control experiment, the fluorescence within Raw 264.7 cells was monitored for 10 min without NO addition. The direct NO mappings were obtained after normalizing each pixel by its corresponding initial intensity. All fluorescence images were obtained with 1-s acquisition using 658 nm excitation (35 mW). (c) Real-time tracking of NIR fluorescence response within Raw 264.7 cells for solutions of NO (5 and  $0.5 \mu\text{M}$ ). The fluorescence intensity is a value from an entire picture plane. (d) A mouse placed on the optical stage of a NIR fluorescence spectrometer and fluorescence response to NO ( $60 \mu\text{M}$ ) within the mouse. A laser beam focused on the abdomen side of the mouse, where the dialysis membrane loaded with the SWNT DAP-dex solution was inserted. The spectra were background-subtracted and obtained with 30-s signal acquisition at 785 nm excitation.<sup>99–101</sup>

carbon-based QDs. Clusters of carbon atoms prepared by bottom-up carbonization<sup>102</sup> and top-down etching<sup>103</sup> methods have successfully tuned the emission color from blue to red. Commonly, carbon-based NPs possess an excitation-dependent photoluminescence (PL) shift for multicolor imaging applications; the emission peaks move to NIR

wavelengths when the excitation wavelength is shifted to red.<sup>104</sup> Li *et al.*<sup>105</sup> showed a complex synthesis procedure of one-step alkali/acid-assisted ultrasonic treatment with a glucose precursor to fabricate NIR-excited NIR carbon NPs. Tao *et al.*<sup>106</sup> obtained carbon-based QDs using an acid treatment on a mixture of CNTs and

graphite. *In vivo* experiments with excitation-dependent fluorescence imaging of carbon-based QDs showed excellent light penetration between 661 and 704 nm. In addition to excitation-dependent methods, the selection of NIR band-pass filters is useful to collect the NIR emission of carbon QDs excited at 400 nm.<sup>107</sup>

Recently, Teng and co-workers reported the excitation-wavelength-independent PL of graphene oxide dots.<sup>108</sup> Their emission peak at 530 nm was far from the NIR region. The authors proposed that the existence of nitrogen dopants possibly reduces vacancy defects and donates electrons to the graphene oxide structure, which allows modifying its electronic structure. Therefore, the next generation of NIR carbon QDs might follow a similar concept of tunable electronic band structures through changing the C, H, O and N compositions<sup>102</sup> in the carbon skeleton.

**NIR organic dyes.** Fluorescent dyes have become an important diagnosis tool for evaluating organ function and enhancing the contrast of cell biological structures. These approaches have primarily focused on the development of *in vitro* assays. In experiments using NIR fluorophores, researchers have demonstrated the excellent evolution of the signal response of protein and DNA sensors (with 680–800 nm excitation and 700–820 nm emission).<sup>109</sup> The additional bi-conjugation to a dye molecule was necessary to improve the sensor sensitivity and selectivity, which in turn increased the signal-to-noise ratio. Alternatively, for angiography or tissue labeling in living organisms, a different approach is to develop NIR dye molecule assays in the NIR spectral region (700–900 nm) to reduce the autofluorescent background and assist image-guided surgery.<sup>110</sup>

Several IRDye and CyDye families have been synthesized. Cy5.5 has strong emission at 690 nm upon excitation at 670 nm. In fact, epidermal growth factor-labeled Cy5.5 was reported to be able to recognize MDA-MB-435 breast cancer xenografts *in vivo*.<sup>111</sup> Another example is the carbocyanine dye indocyanine green (ICG; also known as Cardiogreen), which received Food and Drug Administration approval in 1959 and has its main absorption band between 600 and 900 nm and an emission peak between 750 and 950 nm. This biodegradable dye performed well in clinic trials by enhancing the detection sensitivity, achieving high signal-to-noise ratios, offering a wider dynamic range in many applications and suppressing autofluorescence. As a result, it has been used for many years as a fluorescent indicator in studies involving the heart, liver, lungs and circulation system.<sup>112</sup> In addition to exhibiting increased stability in serum, modified ICG molecules have satisfactory *in vivo* biodistribution and clearance.<sup>110</sup>

In general, the quantum yield of single-photon excited IR fluorophores must be  $>0.01$ .<sup>113</sup> This result is much higher than the multiphoton process for IR fluorophore, which is  $<10^{-8}$ .<sup>114</sup> For deep-tissue functional bioimaging in oncology diagnosis, one-photon excitation of IR fluorophores provides a facile methodology for obtaining strong imaging signals without the need for cellular resolution.<sup>113</sup>

Nevertheless, several issues remain with NIR dyes. First, photo(thermal) instability, aqueous aggregation and non-specific protein binding in blood plasma have limited the biological application of NIR dyes for *in vivo* imaging. These effects deplete the fluorescence quantum efficiency. Second, aggregated and protein-bonded NIR dyes have a short circulation lifespan owing to their rapid clearance from the body, which is incompatible with long-term imaging. A final issue is the low quantum yield of NIR dyes. As a result, a high power density of the laser is required to capture sufficient signal information.

Current approaches include fabricating micelle self-assembly with IR-780 dyes for multimodal image-guided PTT. Nano-assemblies based on a J-aggregation strategy were also discovered to tune the absorption band of fluorophores toward longer wavelengths.<sup>115</sup> IR-825 encapsulated into cationic micelles can be used for imaging-guided photothermal cancer treatment owing to the remarkably enhanced/sharpened NIR absorbance.<sup>116</sup> Song *et al.*<sup>117</sup> designed the co-loading of IR-825 and doxorubicin (DOX) molecules in polyethylenimine/poly(acrylic acid)/PEG, which involved the aggregation-induced absorption band shifting of IR-825 dyes to  $\sim 915$  nm. The authors demonstrated that the NIR nanocomposites were able to provide a stable and repeated photothermal response (915 nm and  $0.35\text{ W cm}^{-2}$ ) as well as the NIR-light-triggered release of DOX, leading to the combination of chemotherapy with PTT.

These advanced results may have the best biocompatibility properties for the long-term usage of a NIR-dye platform for optical and photothermal experiments and excellent efficacy to treat solid tumors in clinical applications.

### Multiphoton-based NPs

Multiphoton microscopy is popular in both *in vitro* and *in vivo* experiments owing to the following advantages: (1) lower phototoxicity to biological materials, (2) high axial resolution for sectioning images, (3) prevention of background interference, (4) preservation of the sample integrity, and (5) a high tissue penetration depth. However, in most cases, the excited electrons in NPs do not have efficient relaxation routes for fluorescence. To obtain sufficiently large imaging contrast, enhancement by unique material properties is necessary. Below we review recent progress in multiphoton processes and uses in various nanomaterial systems.

**Au, Ag and Cu NPs.** The NIR SPR absorption of anisotropic gold, silver and copper NPs can greatly enhance the NIR local field and thus the multiphoton luminescence originally weak in single-photon excitation.<sup>118</sup> Well-known gold nanorods and Au nanocages usually possess surface plasmon frequency in the NIR. The excitation wavelength for these gold NPs is determined by their size/shape effects, porosity structure and dopant composition.<sup>119,120</sup>

When a pulsed laser resonantly excited gold-based NPs in the SPR band, they are able to perform wavelength UC and produce intense nonlinear optical signals, such as second harmonic generation (SHG), TPF and third harmonic generation (THG).<sup>18</sup> Except for SPR absorption, the band-to-band transition states can also enhance the yield of nonlinear optical processes. Previous studies have shown that the electronic states of the d-sp band transition of gold have a vital role in the multiphoton excited emissions when the pulsed excitation energy matches the local field enhancement at the surface plasmon frequency.<sup>121</sup> Indeed, the observed two-photon luminescence (TPL) imaging of Au NRs is approximately 100 times stronger than fluorescence imaging with fluorescein isothiocyanate molecules.<sup>122</sup>

By manipulating the illumination fluence and excitation durations, apoptosis and necrosis of cancer cells have been achieved when cells were labeled with gold nanorods. A low laser power of  $1\text{ mW}$  ( $27.8\text{ W cm}^{-2}$ ) is sufficient to induce both processes. With conjugation to antibodies antiepidermal growth factor receptor, the gold-based NPs could be used for the targeted TPF optical imaging of cancerous cells with a 760–800 nm pulse laser and a duration between 100 and 250 fs.<sup>123</sup> The antibody-conjugated Au nanocages can be attached on the surface of the cells through antibody–antigen binding, thereby enabling the quantification of antibodies immobilized on each nanocage.

In 2000, Xia and co-workers utilized a NIR-II laser at 1290 nm to excite AuAg nanocages and investigated the three-photon luminescence at a low power of 2.4 mW.<sup>120</sup> The authors observed lower autofluorescence background from tissues and cells using a TPL microscope, and they also found that the emission intensity of AuAg nanocages was one order of magnitude stronger than that of Au and Ag NPs. This difference was attributed to the Au–Ag ratio of the alloy composites.

By manipulating the shapes of metallic NPs, the structural asymmetry could result in permanent dipoles in materials and greatly enhance the nonlinear optical efficiencies. For example, the synthesis of Ag–Au triangular nanoplates allowed achieving a twofold higher two-photon absorption (TPA) cross-section when compared with that of Au nanorods.<sup>124</sup> The generation of a strong emission band and excitation wavelength-dependent TPL spectra was observed. The authors reported a strong emission enhancement when the excitation wavelength matched the localized surface plasmon resonance absorbance and the Ag–Au alloy composition. In fact, Li *et al.*<sup>125</sup> reported three-photon luminescence for the nonlinear optical properties of triangular Au/Ag nanoboxes with a different localized surface plasmon resonance. Three-photon luminescence imaging was successfully performed to image the blood vessels of mice and had negligible photothermal toxicity.

In 2009, Chandra and Das<sup>126</sup> utilized polarization-resolved hyper-Rayleigh scattering to probe the origin of second-order nonlinear optical properties in copper NPs. They evaluated the size/wavelength ( $\lambda$ ) of light and found that the SHG of copper NPs closely resembles that of gold but not that of silver. Compared with gold and silver NPs,<sup>127</sup> studies of the size and shape effects of copper NPs have rarely been reported because of their air-sensitive behavior and the loss of fluorescence. Gao and co-workers overcame this problem by developing a peptide–Cu cluster system, which allowed the emission of blue TPF at 460 nm with excitation using a femtosecond laser at 750 nm.<sup>128</sup> However, the development of multiphoton copper NPs is still in the early stages for their synthesis and applications. Several challenges need to be addressed, for example, air/H<sub>2</sub>O stability against degradation,<sup>129</sup> a rigid capping structure with robust photon stability and multiphoton emission at NIR wavelengths.

### Si-based NPs

In bulk, silicon can produce PL from the direct band gaps of 4.2 and 3.4 eV and the indirect band gap of 1.12 eV. Luminescent features of electrochemically prepared porous Si particles have been extensively investigated. In one study, the existence of defects at the particle surface was proposed; these defects provided active sites for the recombination of self-trapped excitons and result in generating bright PL. Greater than 1% of quantum yield was observed.<sup>130</sup> Small-sized Si particles can contribute to size-dependent emission bands based on the quantum confinement size when the Si particle size is smaller than the exciton Bohr diameters (~4.5 nm).<sup>131</sup> Additionally, the surface chemistry with different capping ligands on the Si QDs affected the luminescent band shifting.<sup>132</sup> This single-photon fluorescence contrast has been exploited in confocal microscopy.

Several studies have been conducted on the nonlinear optical response of silicon materials, such as bulk Si, Si embedded in SiO<sub>2</sub> film and porous Si.<sup>133</sup> He *et al.*<sup>134</sup> demonstrated two- and three-photon excitation on 3 nm styrene-grafted and PEG-micelle-encapsulated Si QDs. Theoretically, bulk Si cannot be used to generate SHG using a semiconductor media with centrosymmetry. The resulting inversion symmetry structure makes second-order nonlinear optical processes impossible. However, by modifying the surface of Si

nanocrystals through the addition of different molecules, the atoms at the surface that had centrosymmetry could be broken.<sup>135</sup> Louie and co-workers synthesized manganese-doped silicon QDs (Si<sub>Mn</sub> QDs) and studied potential applications in bioimaging with MRI and NIR-excited TPF imaging. Cell studies showed that the Si<sub>Mn</sub> QD probes could be developed to specifically accumulate in macrophages via a receptor-mediated process using two-photon excitation fluorescence images.<sup>136</sup>

### Quantum dots

Organic dyes suffer from several problems, including hydrophobic structures, photobleaching, difficult derivation and broad emission bands. In general, robust and water-soluble fluorophores are needed in biological environments with enzymatic reactions and acid-based corrosion. Therefore, the most popular CdSe@ZnS nanocrystals, which have size-dependent PL peaks with a high quantum yield, enabled the multicolor imaging of biological samples.<sup>137</sup> In addition to the considerable development of single-photon PL, only a few relevant studies have exploited the multiphoton luminescence of semiconductor QDs.

Meanwhile, it has been demonstrated that the action cross-section of semiconductor QDs is more than two orders of magnitude larger than that of conventional fluorescent probes, such as fluorescein isothiocyanate, and 10 times greater than that of organic molecules that were designed for enhanced TPA.<sup>138</sup> Semiconductor QDs present an extraordinarily high TPA cross-section,  $\sigma = \sim 10^4$ ,<sup>139</sup> and they therefore hold a great promise in TPA- and TPF-based bioimaging. For example, by injecting CdSe@ZnS nanocrystal QDs up to 1  $\mu\text{m}$ , Larson *et al.*<sup>139</sup> were able to obtain an image of the projected vasculature through a 250- $\mu\text{m}$ -thick region within the animal tissue. Accordingly, the blood flow velocity and heart rate were detectable using nonlinear optical microscope technology. The authors determined that the structural detail in imaging was promoted after loading the CdSe@ZnS nanocrystal QDs. Another example is the use of multi-QDs embedded in PMMA-co-MAA nanospheres, which showed extremely high brightness (TPA cross-section up to  $6.23 \times 10^6$  GM).<sup>140</sup> *In vitro* and *in vivo* experiments provided evidence of a superior signal-to-background ratio (> 100) in cellular imaging as well as a deeper penetration depth for tissue imaging.

Moreover, it has previously been shown that the CdSe-based QDs could be used as environmental temperature sensors through one-photon excitation. Subsequently, the Capobianco and García Solé groups reported that the multiphoton emission peaks were temperature sensitive (800 nm and 100 fs) and presented an intracellular temperature gradient in a single living cell, providing a good strategy for live thermal imaging.<sup>141</sup> CdSe/ZnSe QDs modified with amino triphenylamine dendrons and E<sub>2</sub>Zn<sub>2</sub>SOD are chemical probes that are highly sensitive to changes in intracellular Cu<sup>2+</sup> levels under two-photon excitation at 800 nm.<sup>142</sup> This two-photon sensor system exhibited a broad linear range ( $10^{-7}$ – $10^{-3}$  M) and low detection limit down to ~10 nm.

Nevertheless, a significant problem related to the use of CdSe@ZnS nanocrystals is the potential risk for non-specific accumulation of toxic metal ions in the biological environment. To improve their biocompatibility and metabolism, Cd- and Te-free semiconductor nanocrystals have attracted considerable attention and are currently the state-of-the-art for next-generation QDs. The most successful example is ZnS nanocrystals doped with Mn(II) ions. The energy transformation from the band gap (~3.97 eV) of the ZnS QDs to the <sup>4</sup>T<sub>1</sub> state of the Mn(II) ions results in emission at 580 nm based on the Mn(II)-Td transition between <sup>4</sup>T<sub>1</sub> and <sup>6</sup>A<sub>1</sub>.<sup>143</sup> Following a nonlinear

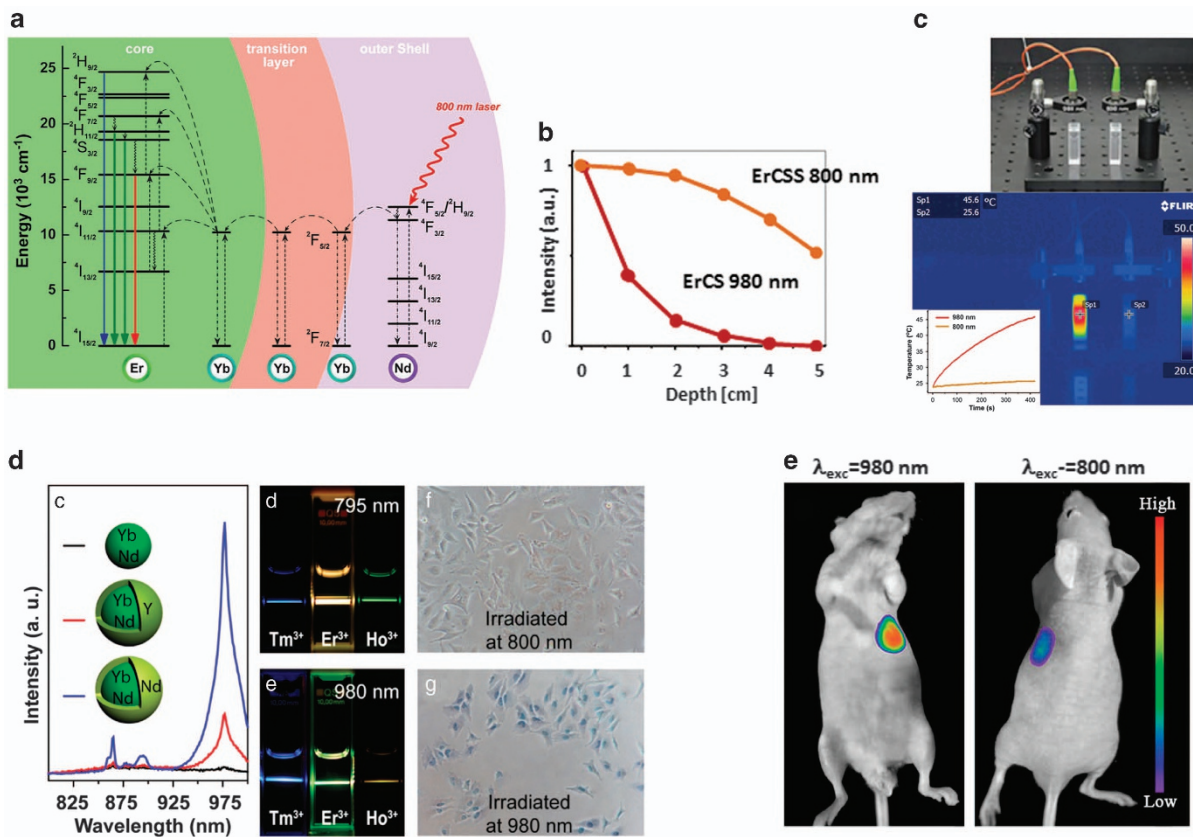


**Figure 11** (a) Energy-transfer mechanisms in the quenching-shield sandwich nanoparticle upon 800 nm diode-laser excitation. (b) The UC emission intensities of the Nd-sensitized sample (orange, 16 mg ml<sup>-1</sup>, excited by a 4 W cm<sup>-2</sup>, 800 nm diode laser) and the Yb-sensitized sample (dark red line, 25 mg ml<sup>-1</sup>, excited by a 4 W cm<sup>-2</sup>, 980 nm diode laser) as a function of penetration depth in water. The concentrations of the Nd-sensitized sample and the Yb-sensitized sample were adjusted to gain the same initial emission intensity. (c) Temperature-distribution image recorded after 7 min irradiation (Sp1: 980 nm,  $T=45.6\text{ }^{\circ}\text{C}$ ; Sp2: 800 nm 25.6 °C; 20 W cm<sup>-2</sup>). Inset: Time-resolved temperature curves. (d) Near-IR photoluminescence spectra (c), images (d, e)—activator emissions (Tm 0.5%, Er 0.5%, Ho 1%) for Nd<sup>3+</sup>-sensitized and Yb<sup>3+</sup>-sensitized nanoparticles under 795 and 980 nm irradiation, respectively, at laser power equal 100 mW and optical *in vitro* images (f, g) of trypan-blue treated HeLa cells recorded after irradiation for 5 min at 800 and 980 nm, respectively (6 W cm<sup>-2</sup>). (e) *In vivo* imaging of a nude mouse from the chest side (left) and the back side (right) by imbuing the water soluble NaGdF<sub>4</sub>:Nd/NaYF<sub>4</sub>/NaGdF<sub>4</sub>:Nd, Yb, Er/NaYF<sub>4</sub> NCs to the stomach.<sup>155,158,159</sup>

optical process, UV-light-induced PL of semiconductor nanocrystals accompanied by blue-green autofluorescence can be prevented. Consequently, *in vivo* optical imaging obtains a higher spatial resolution and tissue depth. Interestingly, Hyeon and co-workers employed a Ti:sapphire pulsed laser at 950 nm (140 fs) to induce the anti-Stokes emission of ZnS:Mn nanocrystals at 580 nm owing to the three-photon excitation.<sup>144</sup> This multiphoton fluorescence process of ZnS:Mn nanocrystals has higher resolution than the TPL of fluorescein isothiocyanate and could be applied to obtain a spectral image of the tumor vasculature.

The final multiphoton luminescence example from the QD family is the NIR-II luminescence of designed Ag<sub>2</sub>S QDs. The wide predicted bandgap of 1.1 eV for monoclinic Ag<sub>2</sub>S encourages researchers to aim at synthesizing small Ag<sub>2</sub>S QDs for efficient NIR emission.<sup>145</sup> The first demonstration of the NIR emission at 1058 nm of Ag<sub>2</sub>S QDs under excitation of 785 nm was reported by Wang and co-workers.<sup>145</sup> With a slight synthesis modification by changing the solvent system, the same group found that Ag<sub>2</sub>S QDs showed strong PL at 1200 nm, and targeted-mediated cellular imaging was demonstrated in the NIR II window.<sup>146</sup> The authors continuously worked on the Ag<sub>2</sub>S conjugated with amine-functionalized six-armed PEG and dihydrolipoic acid, which exhibited an EPR effect on tumor vasculature in mice bearing

xenograft 4T1 tumors according to a steady increase of NIR II fluorescence.

#### Lanthanide-doped upconverting NPs (UCNPs)

The optical properties of lanthanide ions have been known for many years,<sup>147</sup> however, their biomedical potential was revealed when the NP synthesis was developed to reproducibly obtain 8–30 nm diameter colloidal NPs and when suitable biofunctionalization protocols were optimized.<sup>148–150</sup> The great advantages of lanthanide NPs are their<sup>151–153</sup> narrowband absorption/emission spectra (see Figure 2d), which are suitable for multiple labeling and ratiometric biosensors. Moreover, relatively efficient anti-Stokes NIR-to-Vis UC is suitable to diminish both tissue autofluorescence and light scattering. This UC process is far more efficient in quantum terms than other anti-Stokes processes, including TPA and nonlinear effects, when the number of emitted photons is related to the absorbed photons.<sup>154</sup> This is because the real electronic states of lanthanides are involved in multiphoton absorption by sensitizer ions (usually Yb<sup>3+</sup>), which enables a ladder-like population of higher excited states of the activator (Tm, Er or, less frequently, Ho). Another interesting feature of lanthanides is their long luminescence decays (suitable for rejecting the background signal in time-gated mode) and the almost perfect photo-stability of such lanthanide-doped biolabels.<sup>153</sup> Neither photo-blinking nor photo-

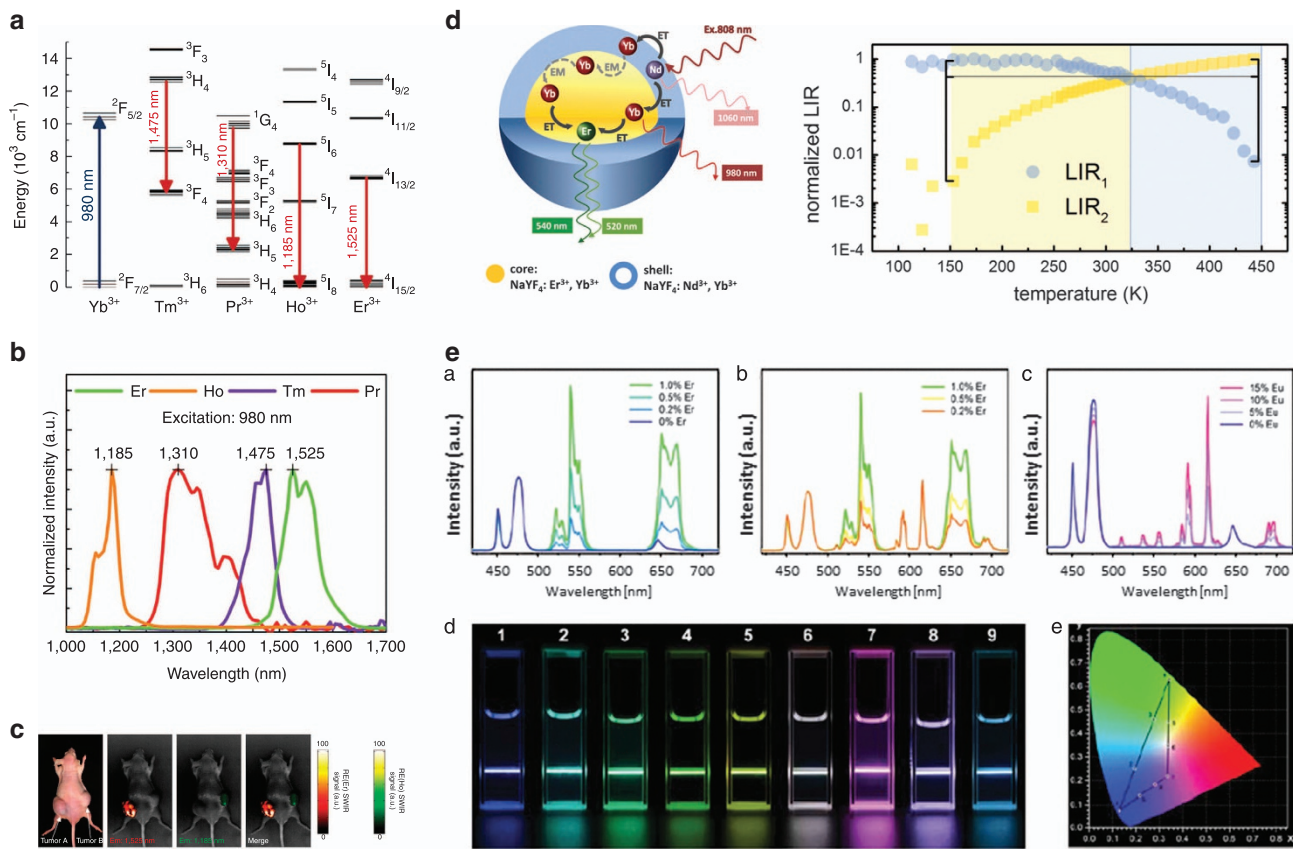


**Figure 12** Lanthanide doped downconverting and upconverting nanoparticles working under NIR photoexcitation and Vis/NIR emission. (a) Schematic illustration of energy levels and (b) emission spectra of Tm, Pr, Ho and Er emission in SWIR region as well as (c) demonstration of multispectral imaging *in vivo* of dorsal aspect in mouse xenografts after Er- and Ho-doped rare-earth probes were separately injected into tumor sites.<sup>167</sup> (d) Idea of broadening the sensitivity range of the ratiometric optical nano-thermometer upon irradiation of YbEr@YbNd ACAS UC nanoparticles with 808 nm photoexcitation—the temperature-sensitive core YbEr energy upconversion and shell Nd → Yb energy transfer are responsible for temperature sensitivity in different temperature ranges.<sup>160</sup> (e) Multicolor emission of (a) NaGdF4:Yb,0.5%Tm, x Er@NaGdF4:Yb, (b) NaGdF4:Yb,0.5%Tm, xEr@NaGdF4:Yb,15% Eu@NaNdF4:Yb and (c) NaGdF4:Yb,0.5% Tm@NaGdF4:Yb,xEu@NaNdF4:Yb colloidal solution of upconverting active-core-active-shell lanthanide-doped nanoparticles.<sup>155</sup> (d) and (e) represent the pictures of up-conversion and the corresponding CIE coordinates, obtained in colloidal solutions of active-core-active-shell UCNPs (a-c).

bleaching has been observed in these materials. These properties offer lanthanide-based tools for applications requiring long observation times, such as studying time-dependent processes or tracing such biofunctionalized labels circulating within living organisms. Recently, through intelligent chemical NP architecture design, by individually doping of core-(multiple)shell NPs (so called active-core-active-shell UCNPs) with lanthanide, many new possibilities have been opened. For example, the excitation wavelength has been shifted from typically 980 nm (matching Yb<sup>3+</sup> absorption) to ~800 nm (matching Nd<sup>3+</sup> absorption) (Figure 11a), at which the water absorption is significantly (that is, ~25 times) less efficient, whereas the absorption cross-section of the respective sensitizers can be as high as or higher than (that is, 5 times larger for 20 mol% Nd<sup>3+</sup> in the shell vs 30 mol% Yb<sup>3+</sup> in the core) that of the Yb<sup>3+</sup>-sensitized UCNPs.<sup>155–158</sup> Such YbA@YbNd (A=Er, Tm, Ho and so on) C-S UCNPs enabled deeper penetration depth (60% higher in water, ~10% in tissues) of 800 vs 980 nm wavelength (Figure 11b), and less light-induced heating definitely occurred. For example, less heating (and less damage to cells), that is,  $\Delta T = 20\text{ }^{\circ}\text{C}$  and  $\Delta T = 7\text{ }^{\circ}\text{C}$ , occurred for 800 nm compared with 980 nm photoexcitation at the same excitation power levels of 20 and 6 W cm<sup>-2</sup>, respectively, for water and tissue experiments (Figures 11c–e).<sup>155,159</sup> Additionally, purpose designed active-core-active-shell lanthanide-doped NPs enabled fine-tuning of

their spectroscopic properties, which, due to the interaction of activating ions with multiple excited states of Nd<sup>3+</sup> sensitizers, have not been available in homogeneously doped materials. Examples of such novel possibilities include broadening the temperature sensitivity range of nanothermometers (Figure 11d)<sup>160</sup> or generating different spectral features from unusual lanthanide activators (for example, Tb<sup>3+</sup> emitting at 540 and 580 nm and Eu<sup>3+</sup> at 580 and 620 nm—Figure 11e), thus enabling the creation of more individual spectral signatures for multiple labeling.<sup>161,162</sup>

Although the lanthanide-based UC mechanism is more efficient than other anti-Stokes phenomena, this anti-Stokes NIR-to-VIS/NIR is not very efficient in absolute terms.<sup>163</sup> This is especially true for NPs where both the sensitizer and activator ions are susceptible to surface quenching.<sup>164</sup> Fortunately, lanthanide materials also have valuable Stokes emissions in the NIR spectral regions (Figures 12a–c),<sup>165</sup> which have been used for imaging in the NIR biological transmission window NIR,<sup>166,167</sup> in intentional light-to-heat and heat-to-temperature<sup>168–171</sup> readout features in single (Figure 12d) or hybrid NP-based ‘devices’. There are numerous comprehensive review articles of the physics, spectroscopy and biomedical applications or nanotoxicity of lanthanide-doped NPs, and thus the readers are referred to these articles for further information.<sup>153,172–180</sup>

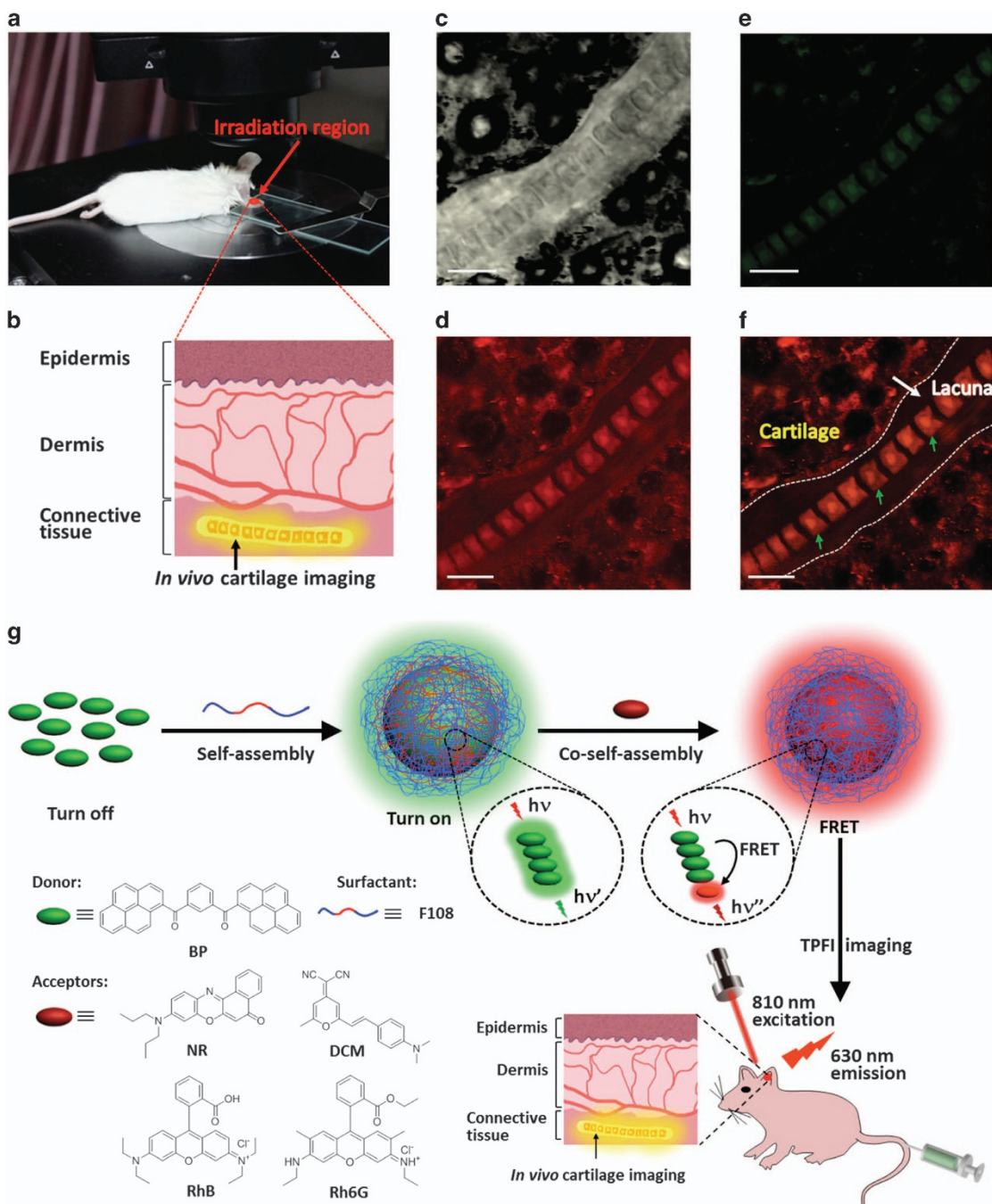


**Figure 13** BP-NR-based TPFI for the cartilage of mice *in vivo*. **(a)** Experimental settings for cartilage TPFI in the ear of mice. **(b)** The anatomic illustration of mice auricle. Intravitral TPFI of BP-NR-stained cartilage in the ear of mice at 10 min postinjection via tail vein under the excitation at 810 nm. TPFI of **(c)** bright field, **(d)** red channel (emission collected at 575–630 nm for BP-NR), **(e)** green channel (emission collected at 495–540 nm for BP) and **(f)** the merged image of (c–e). Scale bar: 20  $\mu$ m. The lacuna is outlined by white dotted lines and chondrocytes are indicated by green arrows. **(g)** Schematic illustration of a FRET-based co-assembled nanosystem as a TPFI contrast agent *in vivo*. The BP nanoaggregates as donors and four different dyes (that is, NR, DCM, RhB and Rh6G) as acceptors were utilized to construct the highly efficient FRET nanosystems.<sup>206</sup>

#### Iron oxide NPs

In 2006, Hashimoto and co-workers extensively investigated the third-order nonlinear optical properties of synthetic  $\alpha$ -Fe<sub>2</sub>O<sub>3</sub>,  $\gamma$ -Fe<sub>2</sub>O<sub>3</sub> and Fe<sub>3</sub>O<sub>4</sub> with a laser light of 1.9  $\mu$ m ( $\sim$ 0.65 eV). According to Miller's rule, the  $\chi^{(3)}$  values of  $3.9 \times 10^{-12}$ ,  $1.4 \times 10^{-12}$  and  $3.1 \times 10^{-12}$  esu are predicted for  $\alpha$ -Fe<sub>2</sub>O<sub>3</sub>,  $\gamma$ -Fe<sub>2</sub>O<sub>3</sub> and Fe<sub>3</sub>O<sub>4</sub> thin films, respectively.<sup>181</sup> These values are larger than those obtained for various metal oxides (for example, SiO<sub>2</sub>, SnO<sub>2</sub> and TiO<sub>2</sub>) with larger band gaps. The band

gaps of  $\alpha$ -Fe<sub>2</sub>O<sub>3</sub> and  $\gamma$ -Fe<sub>2</sub>O<sub>3</sub> are close to 1.96 eV, thus providing an additional electronic transition, enhancing the THG process. Huang and co-workers have used the 1230 nm femtosecond lasers to generate THG and broad multiphoton fluorescence from 450 to 900 nm in nano-sized and submicron  $\alpha$ -Fe<sub>2</sub>O<sub>3</sub> and Fe<sub>3</sub>O<sub>4</sub> particles.<sup>21</sup> The NIR emission showed a good linear correlation with the iron oxide particle's molar extinction coefficient  $\epsilon$  at 1230 nm. We also demonstrated that the polymer-modified surface of 22-nm truncated

octahedral magnetite exhibited a high  $\epsilon$  at 1230 nm, thereby resulting in strong TPF. Compared with Au nanorods (which have an aspect ratio of ~3.9) and Au/Ag nanocages,<sup>120</sup> 22 nm magnetite and 440 nm Fe<sub>3</sub>O<sub>4</sub> particles have a potential emission wavelength >700 nm for deep tissue imaging. In the same work, the downstream multiphoton process enabled the easy visualization of A549 lung cancer cells, which accumulate both large and small Fe<sub>3</sub>O<sub>4</sub> nanomaterials, with either THG or TPF microscopy.

### Multiphoton metal oxide NPs

Solid metal oxides are robust and stable in extreme conditions, such as oxidative and corrosive environments. As a result, they are biocompatible, non-toxic and stable against photobleaching, which makes them promising nonlinear optical agents for long-term imaging. Solid metal oxides with nonlinear optics have been established as an attractive imaging tool for molecular imaging in cells and tissue using NIR excitation. Recently, the SHG properties of several crystals were studied, including barium titanate (BaTiO<sub>3</sub>)<sup>182</sup> zinc oxide (ZnO)<sup>183</sup> KTiOPO<sub>4</sub>,<sup>184</sup> LiNbO<sub>3</sub><sup>185</sup> and PbTiO<sub>3</sub>.<sup>186</sup>

Kachynski *et al.*<sup>183</sup> reported folic-acid-modified ZnO nanocrystals to selectively bind to KB oral cancer cells. Consequently, the intracellular accumulation of the targeted ZnO nanocrystals in live tumor cells could be directly monitored using nonlinear optical microscopy. No significant phototoxicity was obtained with the excitation of a 1064 nm picosecond laser.<sup>187</sup> However, the heating effect caused cell implosion in plant tissues when the laser light wavelength shifted to 710 nm, which was followed by TPA. This wavelength selection is necessary to avoid damage to biological tissues.

Various sizes of BaTiO<sub>3</sub> colloidal NPs were developed, and both their nonlinear optical properties and their *in vitro* and *in vivo* biocompatibility were studied. Compared with other metal oxide materials, inert BaTiO<sub>3</sub> colloidal NPs have superior biocompatibility and efficient contrast for *in vitro* and *in vivo* bioimaging. Imaging examples include mouse-tail tissue,<sup>188</sup> single-cell-stage zebrafish embryos,<sup>182</sup> 3D non-specific labeling of HeLa cells<sup>189</sup> and targeted bioimaging with an immunoglobulin G antibody.<sup>190</sup>

In addition to the popular ZnO and BaTiO<sub>3</sub> NPs, cubic LiNbO<sub>3</sub> NPs and colloidal KTiOPO<sub>4</sub> (KTP) nanocrystals emitted SHG that peaked at 520 nm (with a pulsed laser at 1040 nm) and 512 nm (1024 nm wavelength, 80 MHz repetition rate and 100 fs pulse duration), respectively, which could be used to track mice macrophages.<sup>185</sup> Considering their biocompatibility, the cytotoxicity of five harmonic NPs (KNbO<sub>3</sub>, LiNbO<sub>3</sub>, BaTiO<sub>3</sub>, KTP and Zn) was dose dependent on human adenocarcinoma (A549), adenosquamous carcinoma (HTB-178), lung squamous carcinoma (HTB-182) and non-tumoral BEAS-2B cells.<sup>191</sup> The optical properties of these NPs in harmonic conversion are very similar. However, BaTiO<sub>3</sub> is the most biocompatible in these four different cell lines, whereas ZnO HNPs have high cytotoxic effects, even after short incubation times with these cells.

### NIR-absorbing organic materials: dyes and polymers

Organic dyes and polymer-evolved NIR emission through single-photon and nonlinear optical processes relied on their  $\pi$ -conjugated structure.<sup>109,192,193</sup> The presence of intrinsic anisotropic symmetry in the molecular structures can contribute to SHG.<sup>192</sup> A comprehensive overview of the organic materials with a third-order nonlinear relationship can be found elsewhere.<sup>193</sup>

Several commercially available NIR dyes, including ICG (Cardio-green), DTTC (3,3'-diethylthiatricarbocyanine perchlorate), IR-140 and Styryl 9 M, have two-photon optical properties upon excitation at

1552 nm.<sup>194</sup> Niko *et al.*<sup>195</sup> demonstrated that a synthetic pyrene derivative (4,4'-(1E,1'E)-(3,8-dibutylpyrene-1,6-diyl)bis(ethene-2,1-diyl))bis(1-methylpyridin-1-i um) has an acceptor- $\pi$ -acceptor structure with a large TPA cross-section (1100–1 GM) at 950 nm and 380 GM at 1050 nm. Compared with other NIR dyes, this synthetic pyrene derivative exhibited higher fluorescence quantum yields, which enabled TPF microscope imaging of stained Hek293 cells. To combine the chelating behavior, organic dyes have been designed as fluorescence reporters for sensing metal ions, F<sup>−</sup> ions,<sup>196</sup> oxygen,<sup>197</sup> dopamine<sup>198</sup> and cytokines<sup>199</sup> in two-photon microscopy.

Owing to their unique photophysical properties, square Pt (II) complexes have also been investigated, and their nonlinear optics have been explored.<sup>200</sup> Recently, Tian and co-workers synthesized a novel analogous cis-platinum complex (TDPt) with strong TPA properties.<sup>201</sup> This complex material could be used as a dual-functional agent in imaging and as a chemical drug. The extremely high cross-section value 14 212 GM of TDPt is valuable for further TPA research.

In addition to the multiphoton fluorescence of organic materials in bioimaging (for example, porphyrin-functionalized mesoporous organosilica),<sup>202</sup> NIR photoirradiation promoted energy transfers from the excited singlet state to the excited triplet state of porphyrins,<sup>203</sup> and organic dyes<sup>204,205</sup> for two-photon PDT have been developed for clinical proposes.

Moreover, Wang and co-workers demonstrated the fluorescence resonance energy transfer (FRET)-based co-assembly of C-dots and different dyes (that is, NR, DCM, RhB and Rh6G) as acceptors that exhibit high tissue penetration using an 810 nm excitation wavelength and TPF at 630 nm (Figure 13).<sup>206</sup> Because the current challenge in TPF for biomedical imaging is to develop extremely bright contrast agents with long wavelength emissions, the authors developed a strategy capable of achieving the modulation of emission wavelength to the NIR range upon two-photon NIR irradiation. This strategy represents a highly emissive and photo-stable contrast agent for deep tissue TPF imaging *in vivo*.

### Carbon-based QDs, graphene and nanotubes

Studies of multiphoton excitation and emission with carbon nanodots and graphitic carbon nanodots are rare.<sup>207,208</sup> One key issue is the broad size distribution of synthetic C-dots. This behavior substantially limits the emission peaks of coherence shifting. Although the particle size randomly affected the luminescent peak positions, C-dots have several advantages, including non-blinking fluorescence emission, water solubility, good cell permeability and excellent biocompatibility. Strong two-photon-induced fluorescence from nitrogen-doped graphene QDs,<sup>209</sup> hydrothermally treated carbon QDs<sup>210</sup> and amorphous carbon dots<sup>211</sup> have been reported in recent years. Xie *et al.* utilized an acid treatment process to exfoliate the obtained porous graphitic-C<sub>3</sub>N<sub>4</sub> into ultrathin nanosheets followed by a NH<sub>3</sub>·H<sub>2</sub>O-assisted hydrothermal treatment into single-layered graphitic-C<sub>3</sub>N<sub>4</sub> QDs.<sup>212</sup> According to the experimental results and theoretical simulations, they found that graphitic-C<sub>3</sub>N<sub>4</sub> QDs emit strong blue fluorescence at 400 nm and green emission under one-photon UV excitation and two-photon excitation at 780 nm. In addition to these successful syntheses of carbon-based QDs, the conduction of TPF microscopy made water-dispersed and biocompatible carbon QDs, which might offer new advantages in biosensing, drug delivery, two-photon photodynamic cancer therapy,<sup>213</sup> cellular tracking<sup>212,214,215</sup> and deep-tissue imaging.<sup>209</sup> Ray *et al.* also reported that graphene oxide featured an extremely high 46 890 GM of TPA for selective two-photon imaging of SK-BR-3 breast tumor cells.<sup>216</sup>

The TPF signal at 630 nm of graphene oxide may be enhanced by the resonance with electronic states.

Owing to the unique surface chemistry of C-dots (that is, the carboxylate groups and  $sp^2$  framework),<sup>217</sup> aromatic molecules (chemical drugs and dyes) tend to adsorb onto C-dots through a set of noncovalent chemical interactions, including electrostatic interactions between carboxylate groups at the C-dot surface and positively charged residues, as well as van der Waals interactions between the hydrophobic moieties of the molecule proteins and C-dots. In fact, Choi *et al.*<sup>218</sup> demonstrated that the ZnPc PSS-capped C-dot composite could be used for dual color bioimaging ( $\lambda_{em} = 461$  nm and  $\lambda_{ex} = 358$  nm for C-dots and  $\lambda_{em} = 665$  nm and  $\lambda_{ex} = 647$  nm for ZnPc) and ZnPc-assisted PDT (10 min with a 660 nm laser at 30 mW cm<sup>-2</sup>). By introducing the two-photon process, a single-wavelength excitation could simultaneously induce deep tissue optical imaging, pH sensing and PDT. For example, Zheng and colleagues designed DOX-conjugated C-dots to perform drug delivery in HeLa cells.<sup>214</sup> Two-photon excitation of 810 nm femtosecond sources on C-dots exhibited emission coupling with the excitation band of DOX, thereby evolving an efficient FRET and generating strong red fluorescence at pH 7.4 for glomerular tissues (z-direction at a depth of 65–300  $\mu$ m), whereas the red color emission was depleted when the particles were delivered to the cell body (pH < 5). Intriguingly, Chen and co-workers employed a two-photon excitation FRET strategy to excite a 5,10,15,20-tetrakis(1-methyl 4-pyridinio) porphyrin PS, which caused HeLa cell death through PDT.<sup>213</sup>

Regarding CNTs, the two-photon excitation spectra of SWNTs were first reported by Dukovic and co-workers.<sup>219</sup> The excitation binding energies of CNTs from two-photon PL were subsequently investigated by the same group<sup>220</sup> and Maultzsch *et al.*<sup>221</sup> However, for nonlinear optical bioimaging, the aggregation and poor solubility of CNTs in aqueous-based environments should be avoided.

### Diamond NPs

TPF microscopy has been demonstrated for *in vitro* cell imaging using fluorescent nanodiamonds.<sup>88,93</sup> By changing the excitation wavelength, different defect centers can be selectively excited. For example, a 875 nm femtosecond source can excite 630 nm fluorescence from the (N-V)<sup>0</sup> centers,<sup>88</sup> whereas a 1060 nm source can excite longer 700 nm fluorescence from the (N-V)<sup>-</sup> centers.<sup>222</sup> These are valuable contrasts for *in vivo* deep tissue microscopies. In fact, the second and third harmonic generation properties of nanodiamonds did not rely on real-state electronic transition. Nanodiamonds have also been studied using 820–1500 nm tunable femtosecond sources.<sup>223</sup> The THG nonlinear susceptibility  $\chi^{(3)}$  ( $3\omega;\omega,\omega,\omega$ ) of FND is approximately  $4 \times 10^{-14}$  esu at 1055 nm,<sup>223</sup> which is relatively smaller than that of glass ( $\sim 10^{-12}$  esu). By contrast, the magnitude of nonlinear susceptibility for four-wave mixing  $\chi^{(3)}$  ( $\omega;\omega,-\omega,\omega$ ) is much higher, which is  $-3 \times 10^{-11}$  esu measured by z-scan.<sup>223</sup> This result indicates strong coherent anti-Stokes Raman scattering signals from nanodiamonds. For non-fluorescent nanodiamond, researchers have already exploited the intrinsically strong C-C sp<sup>3</sup> vibrational resonance at 1332 cm<sup>-1</sup> to demonstrate the coherent anti-Stokes Raman scattering microscopy on a single diamond NP.<sup>224</sup> Because the signal level is proportional to the volume of the NP, the feasible crystal size is approximately 150–300 nm.

### TOXICITY OF NIR NPs

With the growing use of various types of nanomaterials, concerns about their impact on human health and the environment has become the subject of a debate. Available studies and collected knowledge

clearly show that the toxicology of nanomaterials is a serious challenge, and approaches based on classical toxicology are not sufficient to answer fundamental questions.

The major problem is a well-documented fact that the physical/chemical properties represented in nanomaterials differ from that of their bulk counterparts. Furthermore, these properties may change and depend on many factors such as size, charge, shape, coating material, the presence of additives, specific cargo and biodegradability. A slight change in size may significantly affect the biodistribution, clearance and retention of nanomaterials. The high level of variables hampers the elaboration of standardized research protocols and necessitates detailed, tedious and costly case-by-case studies. It has been estimated that thorough toxicity testing of nanomaterials currently used in the ultrasound would cost up to \$1.18 billion and would last between 34 and 53 years.<sup>225</sup>

An important consideration is whether a particular nanomaterial has high volume applications and possible environmental pollution must be anticipated or whether it is intended for relatively restricted use, that is, nanomedicines. In the latter case, exploring the possible impact can be narrowed to effects exerted on the human body. Therefore, some degree of hazard can be accepted as it applies to many drugs, that is, the cytostatic properties. Certainly, nanotoxicology must develop new protocols and research methodology to reliably assess the benefit-to-risk ratio to justify the use of new nanomedicines.

The materials described in this review are in the early stages of development as nanomedicines or drug carriers, and toxicological studies are restricted to simple models based on cell lines and small animals, which is understandable considering the high cost and complexity of toxicology studies. Selected candidates will need to undergo detailed studies before authorization for wider use and upgrading the nanotoxicology database. This is especially important for the nanomaterials described here because they are purposely made to be avoid human defense mechanisms to allow them to freely circulate in the body and to target desired sites.

The first aspect when considering the design of nanomaterials for medical applications is the toxicity of the bulk material. Most of the elements or materials employed for the preparation of NIR NPs described herein are considered nontoxic or moderately toxic, such as copper ions. Known toxicity applies to certain metal ions such as cadmium, silver, some noble metals and fluoride ions. In certain cases, the intrinsic toxicity of NP (for example, CuTe NPs) can be diminished by properly engineering the material (for example, encapsulation).<sup>53</sup> However, even materials containing highly toxic components such as cadmium (for example, Cd-based QDs) cannot be excluded on the basis of current results. In contradiction to many studies of cell lines and small animals showing the toxicity of Cd QDs, in experiments on non-human primates, no apparent toxicity was observed.<sup>226</sup> Cadmium was retained in the liver, spleen and kidneys at the end of experiment, but further studies are necessary to estimate clearance and the long-term impact on health. This result also exemplifies the problem of comparing results between different animal models. Moreover, although *in vitro* models are cost effective, easy to perform and popular, they still cannot fully substitute animal studies.

The second consideration is the toxicity of nanomaterials composed of non-toxic elements/materials that arises from the nanoparticulate form of the material. In light of the current studies, no obvious acute toxicity was reported for majority of NIR materials described in this review. However, it must be noted that the available data are not sufficient for drawing solid conclusions. As proven by the example of gold colloid, which is probably the best-studied nanomaterial to date,

these NPs generally are recognized as benign and safe but some forms, that is, specific sizes or with some coating molecules, can be toxic.<sup>227,228</sup> Similarly, lanthanide-doped NPs are basically considered safe, owing to both their chemical composition and size,<sup>180</sup> but their dissolution may potentially become a problem if toxic Gd<sup>3+</sup> ions are part of their composition.

Nanoparticles that escape clearance or degradation may stay deposited in the body for a prolonged period of time, causing long-term toxicity or side effects. However, this problem has been explored sparingly, and it requires further intensive study. Several mechanisms and effects of toxicity caused by NPs on a cellular level are known; for example, inducing reactive oxygen species followed by the oxidation of lipids and proteins components, oxidative stress, protein aggregation and precipitation, growth arrest, Fenton reactions (Fe-based NPs), mitochondrial damage, interference with cell signaling, cell death by apoptosis or necrosis, DNA damage, mutagenesis and others.<sup>229</sup> These toxic effects apply to all materials used for theranostic nanomaterials, but they depend strongly on the design of specific NPs and other conditions, which include numerous factors that must always be considered, for example, (bio)functionalization, size, anisotropy of shape, chemical stability and photo-stability. Moreover, several observations suggest that the route of exposure has a significant impact on the fate and toxicity of NPs. The respiratory tract is a very efficient route of entry for NPs owing to its high surface area and thin mucosal barrier. Internalized NPs are then transported and deposited at systemic sites, including the brain and bones.<sup>230</sup>

Applications of NIR materials for imaging and cancer eradication often rely on systemic injections directly into circulation or into tissues. Data on the distribution and clearance of different types of NPs are still insufficient, but some conclusions may be helpful for the design of new nanomaterials for biomedical purposes. Several studies of the clearance of NPs from the body upon systemic applications showed the ability of NPs to be retained primarily in the liver, spleen and lymph nodes because of the uptake by the RES. Renal clearance is considered an optimal route to clear NPs from circulation, and for that purpose, the hydrodynamic diameter of the particles should not exceed 6 nm. Other studies also showed that the deposition of serum proteins on NP surfaces results in an increase in the diameter (corona formation), which prevents renal filtration. This deposition can be avoided by using a zwitterionic type of coating.<sup>231</sup> Excretion via the bile tract is also a very desirable clearance route, but the NPs must be efficiently internalized by hepatocytes. The second type of phagocytic cells residing in the liver, that is, Kupffer cells, which belongs to the RES, also have significant phagocytic potential, but they are not coupled with the bile tract. Foreign particles engulfed by Kupffer cells are entirely degraded inside the cell; nondegradable particles may then be retained in a body by the RES cells for an extended period of time.<sup>231</sup>

Designing NIR materials for nanomedicine is a challenging task considering that multiple criteria have to ensure safety and effectiveness, even if the 'ideal' agent is impossible to produce. A well-balanced compromise may result in diagnostic and therapeutic agents of great significance for visualizing and combating cancer in increased depths and volumes.

## CONCLUDING REMARKS: THE FUTURE OF NIR NANOMATERIALS

By replacing the single-photon excitation of dye molecules, ultrafast NIR excitation-to-multiphoton and NIR CW laser-UC nanomaterials have mostly expanded the long-standing limitations of optical microscopy that are specific to transition properties and contrast

mechanisms. NIR-active nanomaterials and various optical microscopy systems have improved the anatomical resolution and detection sensitivity for deep-tissue applications. Furthermore, signal responses accessed from NIR excitations have made it possible to detect, identify, characterize and target and treat microenvironments *in vitro* and *in vivo* that were otherwise very difficult to completely access before. This has important repercussions for *in vivo* applications (for example, bioimaging or photomedicine) where the interaction of light with physiological constituents (pigments, proteins and water) should be kept as low as possible.

In this review, we have summarized recent progress in a new classification for NIR-absorbing/emitting nanomaterials involving metal, magnetic, semiconductor, Ln-based and organic materials for *in vivo* bioapplications. We have provided an overview of current results in the interdisciplinary research on NIR-responsive photomedicine and bionanophotonics using innovative UC nanomaterials and NIR-functional NPs. Although NIR-active nanomaterials can push the imaging and action depth deeper, NIR light still encounters optical scattering in tissues and gradually loses its coherence. When NIR light propagates deeper than the scattering attenuation length, it will enter a diffuse photon regime, where the resolution and contrast of optical imaging degrade drastically. Consequently, the ballistic imaging depth of NIR light would be limited to 1–2 mm. To obtain a wider distribution of information for nanomedicine, it is necessary to employ PA signals as the contrast of molecular imaging, for example. The spatial resolution of the PA imaging can be micrometers within the ballistic photon regime and will become several tens of micrometers in the diffuse photon regime. The imaging depth can reach several centimeters with this technique, which is already sufficient to analyze the diffusion of nanomedicines around a tumor beneath the epidermis. Under this scheme, to break the penetration depth limitation, a nanocarrier with dual or multiple contrast capabilities is necessary. Most of the NIR-absorbing nanomaterials described in this review can present PA contrast. However, in PA imaging, pulse energies in the  $\mu\text{J}$  to  $\text{mJ}$  range are required to have a detectable contrast. Such energy level may destroy, melt or deform NPs, and the NIR-absorption features may thus disappear. Therefore, a multiple-contrast NIR-active nanomaterial stable to the excitation in PA imaging is highly desired.

Lanthanide-doped NPs have shown great promise in many biomedical aspects, such as multiple-color and multiple-emission bands for multiplexed detection and labeling different target sites, perfect photo stability for prolonged observations, long luminescence lifetimes for time-gated detection, efficient anti-Stokes emission for NIR photo activation of drugs (for example, UC PDT) and multiple contrast character (fluorescence, MRI/PET/PA). Their major drawbacks, which are currently stimulating intensive ongoing studies, are their absolute low quantum yield (<3%), excitation/emission wavelength optimization (shifting from 980 to 800 nm) and surface quenching in nano-sized materials.

In summary, the optimal NIR materials may need to satisfy several requirements: biocompatibility, engineering flexibility, multi-functionality, and modal capability. The ideal NIR bioprobes must have the following properties:

- High efficiency and spectrally narrow  $\sigma_{\text{ABS}}$  and  $\sigma_{\text{EMI}}$  (cross sections)
- Emission color tunability
- Large Stokes shift
- High photo-stability
- Multimodal detection (Gd ions as MRI contrast)

- Biocompatibility and biospecificity (usually through biofunctionalization)
- Non-toxic (or/and biodegradable)
- Small size
- Ultrasensitive detection (for example, NIR–NIR, time-gated detection)
- Available detection instrumentation

These features will become a ‘road map’ for further developments of novel NP-based drug carriers and imaging/multidetection contrast agents.

## CONFLICT OF INTEREST

The authors declare no conflict of interest.

## ACKNOWLEDGEMENTS

T-ML thanks the financial support from National Health Research Institutes, Taiwan (grant number NHRI-EX105-10427EI), the Ministry of Science and Technology, Taiwan (grant number MoST 104-2627-M-002-018) and the Ministry of Education (the most competitive team program NTU-ERP-105R8956-3). C-CH thanks the financial support from the Ministry of Science and Technology, Taiwan (grant number MoST 103-2113-M-006-011-MY2 and MoST 102-2221-E-006-300-MY3). AB thanks the financial support from the National Science Centre under Grant No. DEC-2012/05/E/ST5/03901. AB and TL thanks the financial support from Wroclaw Research Centre EIT+within the project ‘The Application of Nanotechnology in Advanced Materials’—NanoMat (POIG.01.01.02-02-002/08) financed by the European Regional Development Fund (Operational Programme Innovative Economy, 1.1.2).

- 1 Mura, S., Nicolas, J. & Couvreur, P. Stimuli-responsive nanocarriers for drug delivery. *Nat. Mater.* **12**, 991–1003 (2013).
- 2 Zolnik, B. S., Gonzalez-Fernandez, A., Sadrieh, N. & Dobrovolskaia, M. A. Minireview: nanoparticles and the immune system. *Endocrinology* **151**, 458–465 (2010).
- 3 Ishida, T., Atobe, K., Wang, X. Y. & Kiwada, H. Accelerated blood clearance of PEGylated liposomes upon repeated injections: effect of doxorubicin-encapsulation and high-dose first injection. *J. Controlled Release* **115**, 251–258 (2006).
- 4 Dreher, M. R., Liu, W. G., Michelich, C. R., Dewhirst, M. W., Yuan, F. & Chilkoti, A. Tumor vascular permeability, accumulation, and penetration of macromolecular drug carriers. *J. Natl. Cancer Inst.* **98**, 335–344 (2006).
- 5 Tang, L., Yang, X. J., Yin, Q., Cai, K. M., Wang, H., Chaudhury, I., Yao, C., Zhou, Q., Kwon, M., Hartman, J. A., Dobrucki, I. T., Dobrucki, L. W., Borst, L. B., Leznig, S., Helferich, W. G., Ferguson, A. L., Fan, T. M. & Cheng, J. J. Investigating the optimal size of anticancer nanomedicine. *Proc. Natl. Acad. Sci. USA* **111**, 15344–15349 (2014).
- 6 Hobbs, S. K., Monsky, W. L., Yuan, F., Roberts, W. G., Griffith, L., Torchilin, V. P. & Jain, R. K. Regulation of transport pathways in tumor vessels: role of tumor type and microenvironment. *Proc. Natl. Acad. Sci. USA* **95**, 4607–4612 (1998).
- 7 Cabral, H., Matsumoto, Y., Mizuno, K., Chen, Q., Murakami, M., Kimura, M., Terada, Y., Kano, M. R., Miyazono, K., Uesaka, M., Nishiyama, N. & Kataoka, K. Accumulation of sub-100 nm polymeric micelles in poorly permeable tumours depends on size. *Nat. Nanotechnol.* **6**, 815–823 (2011).
- 8 Sajanlal, P. R., Sreeprasad, T. S., Samal, A. K. & Pradeep, T. Anisotropic nanomaterials: structure, growth, assembly, and functions. *Nano Rev.* **2**, 5883 (2011).
- 9 Zhou, J. F., Meng, L. J. & Lu, Q. H. Core@shell nanostructures for photothermal conversion: tunable noble metal nanoshells on cross-linked polymer submicrospheres. *J. Mater. Chem.* **20**, 5493–5498 (2010).
- 10 Zhang, C., Yin, A. X., Jiang, R. B., Rong, J., Dong, L., Zhao, T., Sun, L. D., Wang, J. F., Chen, X. & Yan, C. H. Time-temperature indicator for perishable products based on kinetically programmable Ag overgrowth on Au nanorods. *ACS Nano* **7**, 4561–4568 (2013).
- 11 Xu, L., Luo, Z. M., Fan, Z. X., Zhang, X., Tan, C. L., Li, H., Zhang, H. & Xue, C. Triangular Ag-Pd alloy nanoprisms: rational synthesis with high-efficiency for electrocatalytic oxygen reduction. *Nanoscale* **6**, 11738–11743 (2014).
- 12 Nehl, C. L., Liao, H. W. & Hafner, J. H. Optical properties of star-shaped gold nanoparticles. *Nano Lett.* **6**, 683–688 (2006).
- 13 Hu, J. T., Odom, T. W. & Lieber, C. M. Chemistry and physics in one dimension: Synthesis and properties of nanowires and nanotubes. *Acc. Chem. Res.* **32**, 435–445 (1999).
- 14 Huang, C. J., Chiu, P. H., Wang, Y. H., Chen, W. R., Meen, T. H. & Yang, C. F. Preparation and characterization of gold nanodumbbells. *Nanotechnology* **17**, 5355–5362 (2006).
- 15 Chen, S.-Y., Cheng, L.-C., Chen, C.-W., Lee, P.-H., Yu, F., Zhou, W., Liu, R.-S., Do, Y.-Y. & Huang, P.-L. NIR-assisted orchid virus therapy using urchin bimetallic nanomaterials in phalaenopsis. *Adv. Nat. Sci. Nanosci. Nanotechnol.* **4**, 045006 (2013).
- 16 Zhan, Q., He, S., Qian, J., Cheng, H. & Cai, F. Optimization of optical excitation of upconversion nanoparticles for rapid microscopy and deeper tissue imaging with higher quantum yield. *Theranostics* **3**, 306–316 (2013).
- 17 Liu, T. M., Yu, J. S., Chang, C. A., Chiou, A., Chiang, H. K., Chuang, Y. C., Wu, C. H., Hsu, C. H., Chen, P. A. & Huang, C. C. One-step shell polymerization of inorganic nanoparticles and their applications in SERS/nonlinear optical imaging, drug delivery, and catalysis. *Sci. Rep.* **4**, 5593 (2014).
- 18 Hu, K. W., Liu, T. M., Chung, K. Y., Huang, K. S., Hsieh, C. T., Sun, C. K. & Yeh, C. S. Efficient near-IR hyperthermia and intense nonlinear optical imaging contrast on the gold nanorod-in-shell nanostructures. *J. Am. Chem. Soc.* **131**, 14186–14187 (2009).
- 19 Welsher, K., Liu, Z., Daranciang, D. & Dai, H. Selective probing and imaging of cells with single walled carbon nanotubes as near-infrared fluorescent molecules. *Nano Lett.* **8**, 586–590 (2008).
- 20 Kam, N. W. S., O’Connell, M., Wisdom, J. A. & Dai, H. J. Carbon nanotubes as multifunctional biological transporters and near-infrared agents for selective cancer cell destruction. *Proc. Natl. Acad. Sci. USA* **102**, 11600–11605 (2005).
- 21 Liao, M. Y., Wu, C. H., Lai, P. S., Yu, J. S., Lin, H. P., Liu, T. M. & Huang, C. C. Surface state mediated NIR two-photon fluorescence of iron oxides for nonlinear optical microscopy. *Adv. Funct. Mater.* **23**, 2044–2051 (2013).
- 22 Makarov, N. S., Lau, P. C., Olson, C., Velizhanin, K. A., Solntsev, K. M., Kieu, K., Kilina, S., Tretiak, S., Norwood, R. A., Peyghambarian, N. & Perry, J. W. Two-photon absorption in CdSe colloidal quantum dots compared to organic molecules. *ACS Nano* **8**, 12572–12586 (2014).
- 23 Yang, K., Zhang, S. A., Zhang, G. X., Sun, X. M., Lee, S. T. & Liu, Z. A. Graphene in mice: ultrahigh in vivo tumor uptake and efficient photothermal therapy. *Nano Lett.* **10**, 3318–3323 (2010).
- 24 Kuo, W. S., Chang, C. N., Chang, Y. T., Yang, M. H., Chien, Y. H., Chen, S. J. & Yeh, C. S. Gold nanorods in photodynamic therapy, as hyperthermia agents, and in near-infrared optical imaging. *Angew. Chem. Int. Ed. Engl.* **49**, 2711–2715 (2010).
- 25 Bachilo, S. M., Strano, M. S., Kittrell, C., Hauge, R. H., Smalley, R. E. & Weisman, R. B. Structure-assigned optical spectra of single-walled carbon nanotubes. *Science* **298**, 2361–2366 (2002).
- 26 Zhou, W., Gao, X., Liu, D. & Chen, X. Gold nanoparticles for in vitro diagnostics. *Chem. Rev.* **115**, 10575–10636 (2015).
- 27 Jaque, D., Maestro, L. M., del Rosal, B., Haro-Gonzalez, P., Benayas, A., Plaza, J. L., Rodriguez, E. M. & Sole, J. G. Nanoparticles for photothermal therapies. *Nanoscale* **6**, 9494–9530 (2014).
- 28 Li, N., Zhao, P. X. & Astruc, D. Anisotropic gold nanoparticles: synthesis, properties, applications, and toxicity. *Angew. Chem. Int. Ed. Engl.* **53**, 1756–1789 (2014).
- 29 Hu, M., Chen, J. Y., Li, Z. Y., Au, L., Hartland, G. V., Li, X. D., Marquez, M. & Xia, Y. N. Gold nanostructures: engineering their plasmonic properties for biomedical applications. *Chem. Soc. Rev.* **35**, 1084–1094 (2006).
- 30 Lucky, S. S., Soo, K. C. & Zhang, Y. Nanoparticles in photodynamic therapy. *Chem. Rev.* **115**, 1990–2042 (2015).
- 31 Tsai, M. F., Chang, S. H. G., Cheng, F. Y., Shanmugam, V., Cheng, Y. S., Su, C. H. & Yeh, C. S. Au nanorod design as light-absorber in the first and second biological windows for in vivo photothermal therapy. *ACS Nano* **7**, 5330–5342 (2013).
- 32 Vijayaraghavan, P., Liu, C. H., Vankayala, R., Chiang, C. S. & Hwang, K. C. Designing multi-branched gold nanochains for NIR light activated dual modal photodynamic and photothermal therapy in the second biological window. *Adv. Mater.* **26**, 6689–6695 (2014).
- 33 American National Standards Institute. *American National Standard for Safe Use of Lasers ANSI Z136.1-2007* (Laser Institute of America: Orlando, FL, USA, 2000).
- 34 Chang, S. S., Shih, C. W., Chen, C. D., Lai, W. C. & Wang, C. R. C. The shape transition of gold nanorods. *Langmuir* **15**, 701–709 (1999).
- 35 Chen, J. Y., Wiley, B., McLellan, J., Xiong, Y. J., Li, Z. Y. & Xia, Y. N. Optical properties of Pd-Ag and Pt-Ag nanoboxes synthesized via galvanic replacement reactions. *Nano Lett.* **5**, 2058–2062 (2005).
- 36 Dos Santos, C. A., Seckler, M. M., Ingle, A. P., Gupta, I., Galdiero, S., Galdiero, M., Gade, A. & Rai, M. Silver nanoparticles: therapeutic uses, toxicity, and safety issues. *J. Pharmaceut. Sci.* **103**, 1931–1944 (2014).
- 37 Huang, X. Q., Tang, S. H., Mu, X. L., Dai, Y., Chen, G. X., Zhou, Z. Y., Ruan, F. X., Yang, Z. L. & Zheng, N. F. Freestanding palladium nanosheets with plasmonic and catalytic properties. *Nat. Nanotechnol.* **6**, 28–32 (2011).
- 38 Huang, X. Q., Tang, S. H., Yang, J., Tan, Y. M. & Zheng, N. F. Etching growth under surface confinement: an effective strategy to prepare mesocrystalline Pd nanocorolla. *J. Am. Chem. Soc.* **133**, 15946–15949 (2011).
- 39 Hu, C. Y., Lin, K. Q., Wang, X. L., Liu, S. J., Yi, J., Tian, Y., Wu, B. H., Chen, G. X., Yang, H. Y., Dai, Y., Li, H. & Zheng, N. F. Electrostatic self-assembling formation of Pd superlattice nanowires from surfactant-free ultrathin Pd nanosheets. *J. Am. Chem. Soc.* **136**, 12856–12859 (2014).
- 40 Niu, W. X., Zhang, W. Q., Firdoz, S. & Lu, X. M. Controlled synthesis of palladium concave nanocubes with sub-10-nanometer edges and corners for tunable plasmonic property. *Chem. Mater.* **26**, 2180–2186 (2014).

- 41 Tang, S. H., Huang, X. Q. & Zheng, N. F. Silica coating improves the efficacy of Pd nanosheets for photothermal therapy of cancer cells using near infrared laser. *Chem. Commun.* **47**, 3948–3950 (2011).
- 42 Huang, X. Q., Tang, S. H., Liu, B. J., Ren, B. & Zheng, N. F. Enhancing the photothermal stability of plasmonic metal nanoplates by a core-shell architecture. *Adv. Mater.* **23**, 3420–3425 (2011).
- 43 Nie, L. M., Chen, M., Sun, X. L., Rong, P. F., Zheng, N. F. & Chen, X. Y. Palladium nanosheets as highly stable and effective contrast agents for *in vivo* photoacoustic molecular imaging. *Nanoscale* **6**, 1271–1276 (2014).
- 44 Tian, Q. W., Tang, M. H., Sun, Y. G., Zou, R. J., Chen, Z. G., Zhu, M. F., Yang, S. P., Wang, J. L., Wang, J. H. & Hu, J. Q. Hydrophilic flower-like CuS superstructures as an efficient 980 nm laser-driven photothermal agent for ablation of cancer cells. *Adv. Mater.* **23**, 3542–3547 (2011).
- 45 Tian, Q. W., Jiang, F. R., Zou, R. J., Liu, Q., Chen, Z. G., Zhu, M. F., Yang, S. P., Wang, J. L., Wang, J. H. & Hu, J. Q. Hydrophilic Cu9S5 nanocrystals: a photothermal agent with a 25.7% heat conversion efficiency for photothermal ablation of cancer cells *in vivo*. *ACS Nano* **5**, 9761–9771 (2011).
- 46 Song, G. S., Han, L. B., Zou, W. W., Xiao, Z. Y., Huang, X. J., Qin, Z. Y., Zou, R. J. & Hu, J. Q. A novel photothermal nanocrystals of Cu7S4 hollow structure for efficient ablation of cancer cells. *Nanomicro Lett.* **6**, 169–177 (2014).
- 47 Tian, Q. W., Hu, J. Q., Zhu, Y. H., Zou, R. J., Chen, Z. G., Yang, S. P., Li, R. W., Su, Q. Q., Han, Y. & Liu, X. G. Sub-10 nm Fe3O4@Cu2-xS core-shell nanoparticles for dual-modal imaging and photothermal therapy. *J. Am. Chem. Soc.* **135**, 8571–8577 (2013).
- 48 Ku, G., Zhou, M., Song, S. L., Huang, Q., Hazle, J. & Li, C. Copper sulfide nanoparticles as a new class of photoacoustic contrast agent for deep tissue imaging at 1064 nm. *ACS Nano* **6**, 7489–7496 (2012).
- 49 Zhou, M., Zhang, R., Huang, M. A., Lu, W., Song, S. L., Melancon, M. P., Tian, M., Liang, D. & Li, C. A chelator-free multifunctional [Cu-64]CuS nanoparticle platform for simultaneous micro-PET/CT imaging and photothermal ablation therapy. *J. Am. Chem. Soc.* **132**, 15351–15358 (2010).
- 50 Yang, K., Yang, G. B., Chen, L., Cheng, L., Wang, L., Ge, C. C. & Liu, Z. FeS nanoplates as a multifunctional nano-theranostic for magnetic resonance imaging guided photothermal therapy. *Biomaterials* **38**, 1–9 (2015).
- 51 Liu, T., Wang, C., Cui, W., Gong, H., Liang, C., Shi, X. Z., Li, Z. W., Sun, B. Q. & Liu, Z. Combined photothermal and photodynamic therapy delivered by PEGylated MoS<sub>2</sub> nanosheets. *Nanoscale* **6**, 11219–11225 (2014).
- 52 Yong, Y., Zhou, L. J., Gu, Z. J., Yan, L., Tian, G., Zheng, X. P., Liu, X. D., Zhang, X., Shi, J. X., Cong, W. S., Yin, W. Y. & Zhao, Y. L. WS<sub>2</sub> nanosheet as a new photosensitizer carrier for combined photodynamic and photothermal therapy of cancer cells. *Nanoscale* **6**, 10394–10403 (2014).
- 53 Li, W. H., Zamani, R., Gil, P. R., Pelaz, B., Ibanez, M., Cadavid, D., Shavel, A., Alvarez-Puebla, R. A., Parak, W. J., Arbiol, J. & Cabot, A. CuTe nanocrystals: shape and size control, plasmonic properties, and use as SERS probes and photothermal agents. *J. Am. Chem. Soc.* **135**, 7098–7101 (2013).
- 54 Scutogella, F., Della Valle, G., Kandada, A. R. S., Zavelani-Rossi, M., Longhi, S., Lanzani, G. & Tassone, F. Plasmonics in heavily-doped semiconductor nanocrystals. *Eur. Phys. J. B* **86**, 154 (2013).
- 55 Abdullae, G. b., Aliyarov, Z. a. & Asadov, G. A. Preparation of Cu<sub>2</sub>Se single crystals and investigation of their electrical properties. *Phys. Status Solidi* **21**, 461–464 (1967).
- 56 Manthiram, K. & Alivisatos, A. P. Tunable localized surface plasmon resonances in tungsten oxide nanocrystals. *J. Am. Chem. Soc.* **134**, 3995–3998 (2012).
- 57 Kalluru, P., Vankayala, R., Chiang, C. S. & Hwang, K. C. Photosensitization of singlet oxygen and *in vivo* photodynamic therapeutic effects mediated by PEGylated W(18)O (49) nanowires. *Angew. Chem. Int. Ed. Engl.* **52**, 12332–12336 (2013).
- 58 Chen, Z. G., Wang, Q., Wang, H. L., Zhang, L. S., Song, G. S., Song, L. L., Hu, J. Q., Wang, H. Z., Liu, J. S., Zhu, M. F. & Zhao, D. Y. Ultrathin PEGylated W18O49 nanowires as a new 980 nm-laser-driven photothermal agent for efficient ablation of cancer cells *in vivo*. *Adv. Mater.* **25**, 2095–2100 (2013).
- 59 Zhou, Z. G., Kong, B. Y., Yu, C., Shi, X. Y., Wang, M. W., Liu, W., Sun, Y. A., Zhang, Y. J., Yang, H. & Yang, S. P. Tungsten oxide nanorods: an efficient nanoplat-form for tumor CT imaging and photothermal therapy. *Sci. Rep.* **4**, 3653 (2014).
- 60 Huo, D., He, J., Li, H., Huang, A. J., Zhao, H. Y., Ding, Y., Zhou, Z. Y. & Hu, Y. X-ray CT guided fault-free photothermal ablation of metastatic lymph nodes with ultrafine HER-2 targeting W18O49 nanoparticles. *Biomaterials* **35**, 9155–9166 (2014).
- 61 Kobayashi, H., Hama, Y., Koyama, Y., Barrett, T., Regino, C. A. S., Urano, Y. & Choyke, P. L. Simultaneous multicolor imaging of five different lymphatic basins using quantum dots. *Nano Lett.* **7**, 1711–1716 (2007).
- 62 Zhang, Y. X., Li, B., Cao, Y. J., Qin, J. B., Peng, Z. Y., Xiao, Z. Y., Huang, X. J., Zou, R. J. & Hu, J. Q. Na<sub>0.3</sub>WO<sub>3</sub> nanorods: a multifunctional agent for *in vivo* dual-modal imaging and photothermal therapy of cancer cells. *Dalton Trans.* **44**, 2771–2779 (2015).
- 63 Xu, W. J., Meng, Z. Q., Yu, N., Chen, Z. G., Sun, B., Jiang, X. Z. & Zhu, M. F. PEGylated Cs<sub>x</sub>WO<sub>3</sub> nanorods as an efficient and stable 915 nm-laser-driven photothermal agent against cancer cells. *RSC Adv.* **5**, 7074–7082 (2015).
- 64 Tian, G., Zhang, X., Zheng, X. P., Yin, W. Y., Ruan, L. F., Liu, X. D., Zhou, L. J., Yan, L., Li, S. J., Gu, Z. J. & Zhao, Y. L. Multifunctional Rb-x WO<sub>3</sub> nanorods for simultaneous combined chemo-photothermal therapy and photoacoustic/CT imaging. *Small* **10**, 4160–4170 (2014).
- 65 Xu, C. J. & Sun, S. H. New forms of superparamagnetic nanoparticles for biomedical applications. *Adv. Drug Deliv. Rev.* **65**, 732–743 (2013).
- 66 Xu, Y. & Schoonen, M. A. A. The absolute energy positions of conduction and valence bands of selected semiconducting minerals. *Am. Mineral.* **85**, 543–556 (2000).
- 67 Wei, X., Xie, T., Peng, L., Fu, W., Chen, J., Gao, Q., Hong, G. & Wang, D. Effect of heterojunction on the behavior of photogenerated charges in Fe<sub>3</sub>O<sub>4</sub>@Fe<sub>2</sub>O<sub>3</sub> nanoparticle photocatalysts. *J. Phys. Chem. C* **115**, 8637–8642 (2011).
- 68 He, Y. P., Miao, Y. M., Li, C. R., Wang, S. Q., Cao, L., Xie, S. S., Yang, G. Z., Zou, B. S. & Burda, C. Size and structure effect on optical transitions of iron oxide nanocrystals. *Phys. Rev. B* **71**, 14045–14056 (2005).
- 69 Sadat, M. E., Baghbador, M. K., Dunn, A. W., Wagner, H. P., Ewing, R. C., Zhang, J. M., Xu, H., Pauletti, G. M., Mast, D. B. & Shi, D. L. Photoluminescence and photothermal effect of Fe3O4 nanoparticles for medical imaging and therapy. *Appl. Phys. Lett.* **105**, 8209–8232 (2014).
- 70 Chen, H. W., Burnett, J., Zhang, F. X., Zhang, J. M., Paholak, H. & Sun, D. X. Highly crystallized iron oxide nanoparticles as effective and biodegradable mediators for photothermal cancer therapy. *J. Mater. Chem. B* **2**, 757–765 (2014).
- 71 Tang, J., Myers, M., Bosnick, K. A. & Brus, L. E. Magnetite Fe3O4 nanocrystals: Spectroscopic observation of aqueous oxidation kinetics. *J. Phys. Chem. B* **107**, 7501–7506 (2003).
- 72 Liao, M. Y., Lai, P. S., Yu, H. P., Lin, H. P. & Huang, C. C. Innovative ligand-assisted synthesis of NIR-activated iron oxide for cancer theranostics. *Chem. Commun.* **48**, 5319–5321 (2012).
- 73 Chu, M. Q., Shao, Y. X., Peng, J. L., Dai, X. Y., Li, H. K., Wu, Q. S. & Shi, D. L. Near-infrared laser light mediated cancer therapy by photothermal effect of Fe3O4 magnetic nanoparticles. *Biomaterials* **34**, 4078–4088 (2013).
- 74 Lin, L. S., Cong, Z. X., Cao, J. B., Ke, K. M., Peng, Q. L., Gao, J. H., Yang, H. H., Liu, G. & Chen, X. Y. Multifunctional Fe3O4@polydopamine core-shell nanocomposites for intracellular mRNA detection and imaging-guided photothermal therapy. *ACS Nano* **8**, 3876–3883 (2014).
- 75 Zhou, Z. G., Sun, Y. A., Shen, J. C., Wei, J., Yu, C., Kong, B., Liu, W., Yang, H., Yang, S. P. & Wang, W. Iron/iron oxide core/shell nanoparticles for magnetic targeting MRI and near-infrared photothermal therapy. *Biomaterials* **35**, 7470–7478 (2014).
- 76 Huang, C. C., Chang, P. Y., Liu, C. L., Xu, J. P., Wu, S. P. & Kuo, W. C. New insight on optical and magnetic Fe3O4 nanoclusters promising for near infrared theranostic applications. *Nanoscale* **7**, 12689–12697 (2015).
- 77 Hong, J. Y., Yoon, H. & Jang, J. Kinetic study of the formation of polypyrrole nanoparticles in water-soluble polymer/metal cation systems: a light-scattering analysis. *Small* **6**, 679–686 (2010).
- 78 Chen, M., Fang, X. L., Tang, S. H. & Zheng, N. F. Polypyrrole nanoparticles for high-performance *in vivo* near-infrared photothermal cancer therapy. *Chem. Commun.* **48**, 8934–8936 (2012).
- 79 Zha, Z. B., Yue, X. L., Ren, Q. S. & Dai, Z. F. Uniform polypyrrole nanoparticles with high photothermal conversion efficiency for photothermal ablation of cancer cells. *Adv. Mater.* **25**, 777–782 (2013).
- 80 Wang, J., Zhou, Z. G., Wang, L., Wei, J., Yang, H., Yang, S. P. & Zhao, J. M. CoFe2O4@MnFe2O4/polypyrrole nanocomposites for *in vitro* photothermal/magnetic-thermal combined therapy. *RSC Adv.* **5**, 7349–7355 (2015).
- 81 Zha, Z. B., Wang, J. R., Qu, E. Z., Zhang, S. H., Jin, Y. S., Wang, S. M. & Dai, Z. F. Polypyrrole hollow microspheres as echogenic photothermal agent for ultrasound imaging guided tumor ablation. *Sci. Rep.* **3**, 2360 (2013).
- 82 Au, K. M., Lu, Z. H., Matcher, S. J. & Armes, S. P. Polypyrrole nanoparticles: a potential optical coherence tomography contrast agent for cancer imaging. *Adv. Mater.* **23**, 5792–5795 (2011).
- 83 Pu, K. Y., Shuhendler, A. J., Jokerst, J. V., Mei, J. G., Gambhir, S. S., Bao, Z. N. & Rao, J. H. Semiconducting polymer nanoparticles as photoacoustic molecular imaging probes in living mice. *Nat. Nanotechnol.* **9**, 233–239 (2014).
- 84 Lim, E. K., Kim, T., Paik, S., Haam, S., Huh, Y. M. & Lee, K. Nanomaterials for theranostics: recent advances and future challenges. *Chem. Rev.* **115**, 327–394 (2015).
- 85 Li, Y. P., Lin, T. Y., Luo, Y., Liu, Q. Q., Xiao, W. W., Guo, W. C., Lac, D., Zhang, H. Y., Feng, C. H., Wachsmann-Hogiu, S., Walton, J. H., Cherry, S. R., Rowland, D. J., Kukis, D., Pan, C. X. & Lam, K. S. A smart and versatile theranostic nanomedicine platform based on nanoporphyrin. *Nat. Commun.* **5**, 4712 (2014).
- 86 Field, J. E. The mechanical and strength properties of diamond. *Rep. Prog. Phys.* **75**, 126505 (2012).
- 87 Gruber, A., Drabenstedt, A., Tietz, C., Fleury, L., Wrachtrup, J. & von Borczyskowski, C. Scanning confocal optical microscopy and magnetic resonance on single defect centers. *Science* **276**, 2012–2014 (1997).
- 88 Yu, S. J., Kang, M. W., Chang, H. C., Chen, K. M. & Yu, Y. C. Bright fluorescent nanodiamonds: no photobleaching and low cytotoxicity. *J. Am. Chem. Soc.* **127**, 17604–17605 (2005).
- 89 Hui, Y. Y., Su, L. J., Chen, O. Y., Chen, Y. T., Liu, T. M. & Chang, H. C. Wide-field imaging and flow cytometric analysis of cancer cells in blood by fluorescent nanodiamond labeling and time gating. *Sci. Rep.* **4**, 5574 (2014).
- 90 Mohan, N., Chen, C. S., Hsieh, H. H., Wu, Y. C. & Chang, H. C. In vivo imaging and toxicity assessments of fluorescent nanodiamonds in *Caenorhabditis elegans*. *Nano Lett.* **10**, 3692–3699 (2010).
- 91 Wu, T. J., Tzeng, Y. K., Chang, W. W., Cheng, C. A., Kuo, Y., Chien, C. H., Chang, H. C. & Yu, J. Tracking the engraftment and regenerative capabilities of transplanted lung stem cells using fluorescent nanodiamonds. *Nat. Nanotechnol.* **8**, 682–689 (2013).
- 92 Mochalin, V. N. & Gogotsi, Y. Wet chemistry route to hydrophobic blue fluorescent nanodiamond. *J. Am. Chem. Soc.* **131**, 4594–4595 (2009).
- 93 Chang, Y. R., Lee, H. Y., Chen, K., Chang, C. C., Tsai, D. S., Fu, C. C., Lim, T. S., Tzeng, Y. K., Fang, C. Y., Han, C. C., Chang, H. C. & Fann, W. Mass production and dynamic imaging of fluorescent nanodiamonds. *Nat. Nanotechnol.* **3**, 284–288 (2008).

- 94 Kam, N. W. S., O'Connell, M., Wisdom, J. A. & Dai, H. Carbon nanotubes as multifunctional biological transporters and near-infrared agents for selective cancer cell destruction. *Proc. Natl. Acad. Sci.* **102**, 11600–11605 (2005).
- 95 Markovic, Z. M., Harhaji-Trajkovic, L. M., Todorovic-Markovic, B. M., Kepic, D. P., Arsikin, K. M., Jovanovic, S. P., Pantovic, A. C., Dramicanin, M. D. & Trajkovic, V. S. In vitro comparison of the photothermal anticancer activity of graphene nanoparticles and carbon nanotubes. *Biomaterials* **32**, 1121–1129 (2011).
- 96 Ghosh, S., Dutta, S., Gomes, E., Carroll, D., D'Agostino, R. Jr., Olson, J., Guthold, M. & Gmeiner, W. H. Increased heating efficiency and selective thermal ablation of malignant tissue with DNA-encased multiwalled carbon nanotubes. *ACS Nano* **3**, 2667–2673 (2009).
- 97 Welsher, K., Sherlock, S. P. & Dai, H. J. Deep-tissue anatomical imaging of mice using carbon nanotube fluorophores in the second near-infrared window. *Proc. Natl. Acad. Sci. USA* **108**, 8943–8948 (2011).
- 98 Bisesi, Jr J. H., Merten, J., Liu, K., Parks, A. N., Afroz, A. R., Glenn, J. B., Klaine, S. J., Kane, A. S., Saleh, N. B., Ferguson, P. L. & Sabo-Attwood, T. Tracking and quantification of single-walled carbon nanotubes in fish using near infrared fluorescence. *Environ. Sci. Technol.* **48**, 1973–1983 (2014).
- 99 Kim, J.-H., Heller, D. A., Jin, H., Barone, P. W., Song, C., Zhang, J., Trudel, L. J., Wogan, G. N., Tannenbaum, S. R. & Strano, M. S. The rational design of nitric oxide selectivity in single-walled carbon nanotube near-infrared fluorescence sensors for biological detection. *Nat. Chem.* **1**, 473–481 (2009).
- 100 Giraldo, J. P., Landry, M. P., Faltermeier, S. M., McNicholas, T. P., Iverson, N. M., Boghossian, A. A., Reuel, N. F., Hilmer, A. J., Sen, F., Brew, J. A. & Strano, M. S. Plant nanobionics approach to augment photosynthesis and biochemical sensing. *Nat. Mater.* **13**, 400–408 (2014).
- 101 Zhang, J., Boghossian, A. A., Barone, P. W., Rwei, A., Kim, J. H., Lin, D., Heller, D. A., Hilmer, A. J., Nair, N., Reuel, N. F. & Strano, M. S. Single molecule detection of nitric oxide enabled by d(AT)15 DNA adsorbed to near infrared fluorescent single-walled carbon nanotubes. *J. Am. Chem. Soc.* **133**, 567–581 (2011).
- 102 Bhunia, S. K., Saha, A., Maity, A. R., Ray, S. C. & Jana, N. R. Carbon nanoparticle-based fluorescent bioimaging probes. *Sci. Rep.* **3**, 1473 (2013).
- 103 Bao, L., Liu, C., Zhang, Z. L. & Pang, D. W. Photoluminescence-tunable carbon nanodots: surface-state energy-gap tuning. *Adv. Mater.* **27**, 1663–1667 (2015).
- 104 Song, Y., Zhu, S. & Yang, B. Bioimaging based on fluorescent carbon dots. *RSC Adv.* **4**, 27184–27200 (2014).
- 105 Li, H., He, X., Liu, Y., Huang, H., Lian, S., Lee, S.-T. & Kang, Z. One-step ultrasonic synthesis of water-soluble carbon nanoparticles with excellent photoluminescent properties. *Carbon* **49**, 605–609 (2011).
- 106 Tao, H., Yang, K., Ma, Z., Wan, J., Zhang, Y., Kang, Z. & Liu, Z. In vivo NIR fluorescence imaging, biodistribution, and toxicology of photoluminescent carbon dots produced from carbon nanotubes and graphite. *Small* **8**, 281–290 (2012).
- 107 Sun, Y. P., Zhou, B., Lin, Y., Wang, W., Fernando, K. A. S., Pathak, P., Meziani, M. J., Harruff, B. A., Wang, X., Wang, H. F., Luo, P. J. G., Yang, H., Kose, M. E., Chen, B. L., Veca, L. M. & Xie, S. Y. Quantum-sized carbon dots for bright and colorful photoluminescence. *J. Am. Chem. Soc.* **128**, 7756–7757 (2006).
- 108 Teng, C.-Y., Yeh, T.-F., Lin, K.-I., Chen, S.-J., Yoshimura, M. & Teng, H. Synthesis of graphene oxide dots for excitation-wavelength independent photoluminescence at high quantum yields. *J. Mater. Chem. C* **3**, 4553–4562 (2015).
- 109 Kobayashi, H., Ogawa, M., Alford, R., Choyke, P. L. & Urano, Y. New strategies for fluorescent probe design in medical diagnostic imaging. *Chem. Rev.* **110**, 2620–2640 (2010).
- 110 Njiojob, C. N., Owens, E. A., Narayana, L., Hyun, H., Choi, H. S. & Henary, M. Tailored near-infrared contrast agents for image guided surgery. *J. Med. Chem.* **58**, 2845–2854 (2015).
- 111 Ke, S., Wen, X. X., Gurfinkel, M., Charnsangavej, C., Wallace, S., Sevick-Muraca, E. M. & Li, C. Near-infrared optical imaging of epidermal growth factor receptor in breast cancer xenografts. *Cancer Res.* **63**, 7870–7875 (2003).
- 112 Namihiwa, T. Indocyanine Green test and its development. *Tokai J. Exp. Clin. Med.* **7**, 419–423 (1982).
- 113 Wishart, G. C., Campisi, M., Boswell, M., Chapman, D., Shackleton, V., Iddles, S., Hallett, A. & Britton, P. D. The accuracy of digital infrared imaging for breast cancer detection in women undergoing breast biopsy. *Eur. J. Surg. Oncol.* **36**, 535–540 (2010).
- 114 Xu, C. T., Svenmarker, P., Liu, H. C., Wu, X., Messing, M. E., Wallenberg, L. R. & Andersson-Engels, S. High-resolution fluorescence diffuse optical tomography developed with nonlinear upconverting nanoparticles. *ACS Nano* **6**, 4788–4795 (2012).
- 115 Wurthner, F., Kaiser, T. E. & Saha-Moller, C. R. J-aggregates: from serendipitous discovery to supramolecular engineering of functional dye materials. *Angew. Chem. Int. Ed. Engl.* **50**, 3376–3410 (2011).
- 116 Song, X. J., Gong, H., Liu, T., Cheng, L., Wang, C., Sun, X. Q., Liang, C. & Liu, Z. J-aggregates of organic dye molecules complexed with iron oxide nanoparticles for imaging-guided photothermal therapy under 915-nm light. *Small* **10**, 4362–4370 (2014).
- 117 Song, X., Zhang, R., Liang, C., Chen, Q., Gong, H. & Liu, Z. Nano-assemblies of J-aggregates based on a NIR dye as a multifunctional drug carrier for combination cancer therapy. *Biomaterials* **57**, 84–92 (2015).
- 118 Durr, N. J., Larson, T., Smith, D. K., Korgel, B. A., Sokolov, K. & Ben-Yakar, A. Two-photon luminescence imaging of cancer cells using molecularly targeted gold nanorods. *Nano Lett.* **7**, 941–945 (2007).
- 119 Knittel, V., Fischer, M. P., de Roo, T., Mecking, S., Leitenstorfer, A. & Brida, D. Nonlinear photoluminescence spectrum of single gold nanostructures. *ACS Nano* **9**, 894–900 (2015).
- 120 Tong, L., Cobley, C. M., Chen, J. Y., Xia, Y. N. & Cheng, J. X. Bright three-photon luminescence from gold/silver alloyed nanostructures for bioimaging with negligible photothermal toxicity. *Angew. Chem. Int. Ed. Engl.* **49**, 3485–3488 (2010).
- 121 Wang, D.S., Hsu, F.Y. & Lin, C. W. Surface plasmon effects on two photon luminescence of gold nanorods. *Opt. Express* **17**, 11350–11359 (2009).
- 122 Li, J. L. & Gu, M. Surface plasmonic gold nanorods for enhanced two-photon microscopic imaging and apoptosis induction of cancer cells. *Biomaterials* **31**, 9492–9498 (2010).
- 123 Au, L., Zhang, Q., Cobley, C. M., Gidding, M., Schwartz, A. G., Chen, J. Y. & Xia, Y. N. Quantifying the cellular uptake of antibody-conjugated Au nanocages by two-photon microscopy and inductively coupled plasma mass spectrometry. *ACS Nano* **4**, 35–42 (2010).
- 124 Sun, J. S., Wang, X. L., Liu, J. F., Wan, P. B., Liao, Q., Wang, F., Luo, L. & Sun, X. M. Highly stable Ag-Au nanoplates and nanoframes for two-photon luminescence. *RSC Adv.* **4**, 35263–35267 (2014).
- 125 Li, K. H., Wang, Y. L., Cai, F. H., Yu, J. X., Wang, S. W., Zhu, Z. F., Chu, L. L., Zhang, H. Q., Qian, J. & He, S. L. Nonlinear optical properties of Au/Ag alloyed nanoboxes and their applications in both *in vitro* and *in vivo* bioimaging under long-wavelength femtosecond laser excitation. *RSC Adv.* **5**, 2851–2856 (2015).
- 126 Chandra, M. & Das, P. K. 'Small-particle limit' in the second harmonic generation from noble metal nanoparticles. *Chem. Phys.* **358**, 203–208 (2009).
- 127 Singh, A. K., Senapati, D., Neely, A., Kolawole, G., Hawker, C. & Ray, P. C. Nonlinear optical properties of triangular silver nanomaterials. *Chem. Phys. Lett.* **481**, 94–98 (2009).
- 128 Wang, Y., Cui, Y., Liu, R., Wei, Y., Jiang, X., Zhu, H., Gao, L., Zhao, Y., Chai, Z. & Gao, X. Blue two-photon fluorescence metal cluster probe precisely marking cell nuclei of two cell lines. *Chem. Commun.* **49**, 10724–10726 (2013).
- 129 Wei, W., Lu, Y., Chen, W. & Chen, S. One-pot synthesis, photoluminescence, and electrocatalytic properties of subnanometer-sized copper clusters. *J. Am. Chem. Soc.* **133**, 2060–2063 (2011).
- 130 Canham, L. T. Silicon quantum wire array fabrication by electrochemical and chemical dissolution of wafers. *Appl. Phys. Lett.* **57**, 1046–1048 (1990).
- 131 Littau, K. A., Szajowski, P. J., Muller, A. J., Kortan, A. R. & Brus, L. E. A luminescent silicon nanocrystal colloid via a high-temperature aerosol reaction. *J. Phys. Chem.* **97**, 1224–1230 (1993).
- 132 Warner, J. H., Rubinstein-Dunlop, H. & Tilley, R. D. Surface morphology dependent photoluminescence from colloidal silicon nanocrystals. *J. Phys. Chem. B* **109**, 19064–19067 (2005).
- 133 Wang, J., Jiang, H. B., Wang, W. C., Zheng, J. B., Zhang, F. L., Hao, P. H., Hou, X. Y. & Wang, X. Efficient infrared-up-conversion luminescence in porous silicon-a quantum-confinement-induced effect. *Phys. Rev. Lett.* **69**, 3252–3255 (1992).
- 134 He, G. S., Zheng, Q. D., Yong, K. T., Erogbogbo, F., Swihart, M. T. & Prasad, P. N. Two- and three-photon absorption and frequency upconverted emission of silicon quantum dots. *Nano Lett.* **8**, 2688–2692 (2008).
- 135 Schriever, C., Bohley, C. & Wehrspohn, R. B. Strain dependence of second-harmonic generation in silicon. *Optics Lett.* **35**, 273–275 (2010).
- 136 Tu, C. Q., Ma, X. C., Pantazis, P., Kauzlarich, S. M. & Louie, A. Y. Paramagnetic, silicon quantum dots for magnetic resonance and two-photon imaging of macrophages. *J. Am. Chem. Soc.* **132**, 2016–2023 (2010).
- 137 Chan, W. C. W., Maxwell, D. J., Gao, X. H., Bailey, R. E., Han, M. Y. & Nie, S. M. Luminescent quantum dots for multiplexed biological detection and imaging. *Curr. Opin. Biotechnol.* **13**, 40–46 (2002).
- 138 Albota, M., Beljonne, D., Bredas, J. L., Ehrlich, J. E., Fu, J. Y., Heikal, A. A., Hess, S. E., Kogej, T., Levin, M. D., Marder, S. R., McCord-Maughon, D., Perry, J. W., Rockel, H., Rumi, M., Subramaniam, C., Webb, W. W., Wu, X. L. & Xu, C. Design of organic molecules with large two-photon absorption cross sections. *Science* **281**, 1653–1656 (1998).
- 139 Larson, D. R., Zipfel, W. R., Williams, R. M., Clark, S. W., Bruchez, M. P., Wise, F. W. & Webb, W. W. Water-soluble quantum dots for multiphoton fluorescence imaging *in vivo*. *Science* **300**, 1434–1436 (2003).
- 140 Fan, Y. Y., Liu, H. L., Han, R. C., Huang, L., Shi, H., Sha, Y. L. & Jiang, Y. Q. Extremely high brightness from polymer-encapsulated quantum dots for two-photon cellular and deep-tissue imaging. *Sci. Rep.* **5**, 9908 (2015).
- 141 Maestro, L. M., Rodriguez, E. M., Rodriguez, F. S., la Cruz, M. C. I., Juarranz, A., Naccache, R., Vetrone, F., Jaque, D., Capobianco, J. A. & Sole, J. G. CdSe quantum dots for two-photon fluorescence thermal imaging. *Nano Lett.* **10**, 5109–5115 (2010).
- 142 Fu, Y., Ding, C. Q., Zhu, A. W., Deng, Z. F., Tian, Y. & Jin, M. Two-photon ratiometric fluorescent sensor based on specific biomolecular recognition for selective and sensitive detection of copper ions in live cells. *Anal. Chem.* **85**, 11936–11943 (2013).
- 143 Ke, J., Li, X. Y., Zhao, Q. D., Hou, Y. & Chen, J. H. Ultrasensitive quantum dot fluorescence quenching assay for selective detection of mercury ions in drinking water. *Sci. Rep.* **4**, 5624 (2014).
- 144 Yu, J. H., Kwon, S. H., Petrasek, Z., Park, O. K., Jun, S. W., Shin, K., Choi, M., Il Park, Y., Park, K., Na, H. B., Lee, N., Lee, D. W., Kim, J. H., Schwille, P. & Hyeon, T. High-resolution three-photon biomedical imaging using doped ZnS nanocrystals. *Nat. Mater.* **12**, 359–366 (2013).
- 145 Du, Y. P., Xu, B., Fu, T., Cai, M., Li, F., Zhang, Y. & Wang, Q. B. Near-infrared photoluminescent Ag<sub>2</sub>S quantum dots from a single source precursor. *J. Am. Chem. Soc.* **132**, 1470–1471 (2010).

- 146 Zhang, Y., Hong, G. S., Zhang, Y. J., Chen, G. C., Li, F., Dai, H. J. & Wang, Q. B. Ag<sub>2</sub>S quantum dot: a bright and biocompatible fluorescent nanoprobe in the second near-infrared window. *ACS Nano* **6**, 3695–3702 (2012).
- 147 Auzel, F. Multiphonon-assisted anti-Stokes and Stokes fluorescence of triply ionized rare-earth ions. *Phys. Rev. B* **13**, 2809–2817 (1976).
- 148 Zijlmans, H. J. M. A. A., Bonnet, J., Burton, J., Kardos, K., Vail, T., Niedbala, R. S. & Tanke, H. J. Detection of cell and tissue surface antigens using up-converting phosphors: a new reporter technology. *Anal. Biochem.* **267**, 30–36 (1999).
- 149 Heer, S., Kompe, K., Gudel, H. U. & Haase, M. Highly efficient multicolour upconversion emission in transparent colloids of lanthanide-doped NaYF<sub>4</sub> nanocrystals. *Adv. Mater.* **16**, 2102–2105 (2004).
- 150 Sedlmeier, A. & Gorris, H. H. Surface modification and characterization of photon-upconverting nanoparticles for bioanalytical applications. *Chem. Soc. Rev.* **44**, 1526–1560 (2015).
- 151 Chen, G. Y., Agren, H., Ohulchansky, T. Y. & Prasad, P. N. Light upconverting core-shell nanostructures: nanophotonic control for emerging applications. *Chem. Soc. Rev.* **44**, 1680–1713 (2015).
- 152 Park, Y. I., Lee, K. T., Suh, Y. D. & Hyeon, T. Upconverting nanoparticles: a versatile platform for wide-field two-photon microscopy and multi-modal *in vivo* imaging. *Chem. Soc. Rev.* **44**, 1302–1317 (2015).
- 153 Gnach, A. & Bednarkiewicz, A. Lanthanide-doped up-converting nanoparticles: Merits and challenges. *Nano Today* **7**, 532–563 (2012).
- 154 Auzel, F. Upconversion and anti-stokes processes with f and d ions in solids. *Chem. Rev.* **104**, 139–173 (2004).
- 155 Zhong, Y., Tian, G., Gu, Z., Yang, Y., Gu, L., Zhao, Y., Ma, Y. & Yao, J. Elimination of photon quenching by a transition layer to fabricate a quenching-shield sandwich structure for 800 nm excited upconversion luminescence of Nd<sup>3+</sup>-sensitized nanoparticles. *Adv. Mater.* **26**, 2831–2837 (2014).
- 156 Wang, Y. F., Liu, G. Y., Sun, L. D., Xiao, J. W., Zhou, J. C. & Yan, C. H. Nd<sup>3+</sup>-sensitized upconversion nanophosphors: efficient *in vivo* bioimaging probes with minimized heating effect. *ACS Nano* **7**, 7200–7206 (2013).
- 157 Wang, F., Deng, R., Wang, J., Wang, Q., Han, Y., Zhu, H., Chen, X. & Liu, X. Tuning upconversion through energy migration in core-shell nanoparticles. *Nat. Mater.* **10**, 968–973 (2011).
- 158 Xie, X. J., Gao, N. Y., Deng, R. R., Sun, Q., Xu, Q. H. & Liu, X. G. Mechanistic investigation of photon upconversion in Nd<sup>3+</sup>-sensitized core-shell nanoparticles. *J. Am. Chem. Soc.* **135**, 12608–12611 (2013).
- 159 Li, X. M., Wang, R., Zhang, F., Zhou, L., Shen, D. K., Yao, C. & Zhao, D. Y. Nd<sup>3+</sup> sensitized up/down converting dual-mode nanomaterials for efficient *in-vitro* and *in-vivo* bioimaging excited at 800 nm. *Sci. Rep.* **3**, 3536 (2013).
- 160 Marciniak, L., Prorok, K., Frances-Soriano, L., Perez-Prieto, J. & Bednarkiewicz, A. A broadening temperature sensitivity range with a core-shell YbEr@YbNd double ratiometric optical nanothermometer. *Nanoscale* **8**, 5037–5042 (2016).
- 161 Prorok, K., Bednarkiewicz, A., Cichy, B., Gnach, A., Misiak, M., Sobczyk, M. & Strek, W. The impact of shell host (NaYF<sub>4</sub>(CaF<sub>2</sub>)) and shell deposition methods on the up-conversion enhancement in Tb(3+), Yb(3+) codoped colloidal alpha-NaYF<sub>4</sub>(4) core-shell nanoparticles. *Nanoscale* **6**, 1855–1864 (2014).
- 162 Prorok, K. P. M., Strek, W. & Bednarkiewicz, A. Energy migration up-conversion of Tb<sup>3+</sup> in Yb<sup>3+</sup> and Nd<sup>3+</sup> co-doped active-core/active-shell colloidal nanoparticles. *Chem. Mater.* **28**, 2295–2300 (2016).
- 163 Boyer, J. C. & van Veghel, F. Absolute quantum yield measurements of colloidal NaYF<sub>4</sub>: Er<sup>3+</sup>, Yb<sup>3+</sup> upconverting nanoparticles. *Nanoscale* **2**, 1417–1419 (2010).
- 164 Arppe, R., Hyppanen, I., Perala, N., Peltomaa, R., Kaiser, M., Wurth, C., Christ, S., Resch-Genger, U., Schaferling, M. & Soukka, T. Quenching of the upconversion luminescence of NaYF<sub>4</sub>:Yb<sup>3+</sup>,Er<sup>3+</sup> and NaYF<sub>4</sub>:Yb<sup>3+</sup>,Tm<sup>3+</sup> nanophosphors by water: the role of the sensitizer Yb<sup>3+</sup> in non-radiative relaxation. *Nanoscale* **7**, 11746–11757 (2015).
- 165 del Rosal, B., Perez-Delgado, A., Misiak, M., Bednarkiewicz, A., Vanetsev, A. S., Orlovskii, Y., Jovanovic, D. J., Dramicanin, M. D., Rocha, U., Kumar, K. U., Jacinto, C., Navarro, E., Rodriguez, E. M., Pedroni, M., Speghini, A., Hirata, G. A., Martin, I. R. & Jaque, D. Neodymium-doped nanoparticles for infrared fluorescence bioimaging: the role of the host. *J. Appl. Phys.* **118**, 143104 (2015).
- 166 Dong, N. N., Pedroni, M., Piccinelli, F., Conti, G., Sbarati, A., Ramirez-Hernandez, J. E., Maestro, L. M., Iglesias-de la Cruz, M. C., Sanz-Rodriguez, F., Juarranz, A., Chen, F., Vetrone, F., Capobianco, J. A., Sole, J. G., Bettinelli, M., Jaque, D. & Speghini, A. NIR-to-NIR two-photon excited CaF<sub>2</sub>: Tm<sup>3+</sup>,Yb<sup>3+</sup> nanoparticles: multifunctional nanoprobes for highly penetrating fluorescence bio-imaging. *ACS Nano* **5**, 8665–8671 (2011).
- 167 Naczynski, D. J., Tan, M. C., Zevon, M., Wall, B., Kohl, J., Kulesa, A., Chen, S., Roth, C. M., Rimann, R. E. & Moghe, P. V. Rare-earth-doped biological composites as *in vivo* shortwave infrared reporters. *Nat. Commun.* **4**, 2199 (2013).
- 168 Bednarkiewicz, A., Wawrzynczyk, D., Nyk, M. & Strek, W. Optically stimulated heating using Nd(3+) doped NaYF<sub>4</sub>) colloidal near infrared nanophosphors. *Appl. Phys. B Lasers Optics* **103**, 847–852 (2011).
- 169 Wawrzynczyk, D., Bednarkiewicz, A., Nyk, M., Strek, W. & Samoc, M. Neodymium(III) doped fluoride nanoparticles as non-contact optical temperature sensors. *Nanoscale* **4**, 6959–6961 (2012).
- 170 Ceron, E. N., Ortgies, D. H., del Rosal, B., Ren, F., Benayas, A., Vetrone, F., Ma, D., Sanz-Rodriguez, F., Sole, J. G., Jaque, D. & Rodriguez, E. M. Hybrid nanostructures for high-sensitivity luminescence nanothermometry in the second biological window. *Adv. Mater.* **27**, 4781–4787 (2015).
- 171 Jaque, D. & Vetrone, F. Luminescence nanothermometry. *Nanoscale* **4**, 4301–4326 (2012).
- 172 Chen, X., Peng, D., Ju, Q. & Wang, F. Photon upconversion in core-shell nanoparticles. *Chem. Soc. Rev.* **44**, 1318–1330 (2014).
- 173 Li, X., Zhang, F. & Zhao, D. Lab on upconversion nanoparticles: optical properties and applications engineering via designed nanostructure. *Chem. Soc. Rev.* **44**, 1346–1378 (2014).
- 174 Liu, G. Advances in the theoretical understanding of photon upconversion in rare-earth activated nanophosphors. *Chem. Soc. Rev.* **44**, 1635–1652 (2014).
- 175 Sun, Y., Feng, W., Yang, P., Huang, C. & Li, F. The biosafety of lanthanide upconversion nanomaterials. *Chem. Soc. Rev.* **44**, 1509–1525 (2014).
- 176 Wang, F. & Liu, X. Recent advances in the chemistry of lanthanide-doped upconversion nanocrystals. *Chem. Soc. Rev.* **38**, 976–976 (2009).
- 177 Hänninen P. & Härmä H. (eds). *Lanthanide Luminescence* (Springer, 2011).
- 178 Auzel, F. Upconversion and anti-Stokes processes with f and d ions in solids. *Chem. Rev.* **104**, 139–174 (2004).
- 179 Kaminskii, A. *Crystalline Lasers: physical Processes and Operating Schemes* (CRC Press, Boca Raton, FL, USA, 1996).
- 180 Gnach, A., Lipinski, T., Bednarkiewicz, A., Rybka, J. & Capobianco, J. Upconverting nanoparticles: assessing the toxicity. *Chem. Soc. Rev.* **44**, 1561–1584 (2015).
- 181 Hashimoto, T., Yamada, T. & Yoko, T. Third-order nonlinear optical properties of sol-gel derived  $\alpha$ -Fe<sub>2</sub>O<sub>3</sub>,  $\gamma$ -Fe<sub>2</sub>O<sub>3</sub>, and Fe<sub>3</sub>O<sub>4</sub> thin films. *J. Appl. Phys.* **80**, 3184 (1996).
- 182 Pantazis, P., Maloney, J., Wu, D. & Fraser, S. E. Second harmonic generating (SHG) nanoprobes for *in vivo* imaging. *Proc. Natl. Acad. Sci. USA* **107**, 14535–14540 (2010).
- 183 Kachynski, A. V., Kuzmin, A. N., Nyk, M., Roy, I. & Prasad, P. N. Zinc oxide nanocrystals for nonresonant nonlinear optical microscopy in biology and medicine. *J. Phys. Chem. C* **112**, 10721–10724 (2008).
- 184 Le Xuan, L., Zhou, C., Slablab, A., Chauvat, D., Tard, C., Perruchas, S., Gacoin, T., Villevalet, P. & Roch, J. F. Photostable second-harmonic generation from a single KTiOPO<sub>4</sub> nanocrystal for nonlinear microscopy. *Small* **4**, 1332–1336 (2008).
- 185 Wang, Y., Zhou, X. Y., Chen, Z., Cai, B., Ye, Z. Z., Gao, C. Y. & Huang, J. Y. Synthesis of cubic LiNbO<sub>3</sub> nanocrystals and their application *in vitro* bioimaging. *Appl. Phys. A Mater. Sci. Process.* **117**, 2121–2126 (2014).
- 186 Joulaud, C., Mugnier, Y., Djanta, G., Dubled, M., Marty, J. C., Galez, C., Wolf, J. P., Bonacina, L. & Le Dantec, R. Characterization of the nonlinear optical properties of nanocrystals by hyper Rayleigh scattering. *J. Nanobiotechnol.* **11**, S8 (2013).
- 187 Urban, B. E., Neogi, P. B., Butler, S. J., Fujita, Y. & Neogi, A. Second harmonic imaging of plants tissues and cell implosion using two-photon process in ZnO nanoparticles. *J. Biophotonics* **5**, 283–291 (2012).
- 188 Grange, R., Lanvin, T., Hsieh, C. L., Pu, Y. & Psaltis, D. Imaging with second-harmonic radiation probes in living tissue. *Biomed. Opt. Express* **2**, 2532–2539 (2011).
- 189 Hsieh, C. L., Grange, R., Pu, Y. & Psaltis, D. Three-dimensional harmonic holographic microscopy using nanoprobes as probes for cell imaging. *Opt. Express* **17**, 2880–2891 (2009).
- 190 Hsieh, C. L., Grange, R., Pu, Y. & Psaltis, D. Bioconjugation of barium titanate nanocrystals with immunoglobulin G antibody for second harmonic radiation imaging probes. *Biomaterials* **31**, 2272–2277 (2010).
- 191 Staedler, D., Magouroux, T., Hadji, R., Joulaud, C., Extermann, J., Schwungi, S., Passemard, S., Kasparian, C., Clarke, G., Gerrmann, M., Le Dantec, R., Mugnier, Y., Rytz, D., Ciepielewski, D., Galez, C., Gerber-Lemaire, S., Juillerat-Jeanneret, L., Bonacina, L. & Wolf, J. P. Harmonic nanocrystals for biolabeling: a survey of optical properties and biocompatibility. *ACS Nano* **6**, 2542–2549 (2012).
- 192 Delaire, J. A. & Nakatani, K. Linear and nonlinear optical properties of photochromic molecules and materials. *Chem. Rev.* **100**, 1817–1845 (2000).
- 193 Nalwa, H. S. Organic materials for 3rd-order nonlinear optics. *Adv. Mater.* **5**, 341–358 (1993).
- 194 Berezin, M. Y., Zhan, C., Lee, H., Joo, C., Akers, W. J., Yazdanfar, S. & Achilefu, S. Two-photon optical properties of near-infrared dyes at 1.55  $\mu$ m excitation. *J. Phys. Chem. B* **115**, 11530–11535 (2011).
- 195 Niko, Y., Moritomo, H., Sugihara, H., Suzuki, Y., Kawamata, J. & Konishi, G. I. A novel pyrene-based two-photon active fluorescent dye efficiently excited and emitting in the 'tissue optical window (650–1100 nm)'. *J. Mater. Chem. B* **3**, 184–190 (2015).
- 196 Zhu, X. Y., Wang, J. X., Zhang, J. J., Chen, Z. J., Zhang, H. X. & Zhang, X. Y. Imaging of fluoride ion in living cells and tissues with a two-photon ratiometric fluorescence probe. *Sensors* **15**, 1611–1622 (2015).
- 197 Roussakis, E., Spencer, J. A., Lin, C. P. & Vinogradov, S. A. Two-photon antenna-core oxygen probe with enhanced performance. *Anal. Chem.* **86**, 5937–5945 (2014).
- 198 Jin, H., Gui, R. J., Wang, Z. H., Zhang, F. F., Xia, J. F., Yang, M., Bi, S. & Xia, Y. Z. Two-photon excited quantum dots with compact surface coatings of polymer ligands used as an upconversion luminescent probe for dopamine detection in biological fluids. *Analyst* **140**, 2037–2043 (2015).
- 199 Yan, H. J., He, L. L., Zhao, W. J., Li, J. S., Xiao, Y., Yang, R. H. & Tan, W. H. Poly beta-cyclodextrin/TDye nanomicelle-based two-photon nanoprobe for caspase-3 activation imaging in live cells and tissues. *Anal. Chem.* **86**, 11440–11450 (2014).
- 200 Chan, C. K. M., Tao, C. H., Tam, H. L., Zhu, N. Y., Yam, V. W. W. & Cheah, K. W. Synthesis, characterization, luminescence, and non-linear optical properties of oxadiazole- and truxene-containing platinum(II) alkynyl complexes with donor-acceptor functionalities. *Inorg. Chem.* **48**, 2855–2864 (2009).
- 201 Zhang, Q., Tian, X. H., Hu, G. J., Shi, P. F., Wu, J. Y., Li, S. L., Zhou, H. P., Jin, B. K., Yang, J. X., Zhang, S. Y. & Tian, Y. P. Dual-functional analogous cis-platinum complex

- with high antitumor activities and two-photon bioimaging. *Biochemistry* **54**, 2177–2180 (2015).
- 202 Mauriello-Jimenez, C., Croissant, J., Maynadier, M., Cattoen, X., Man, M. W. C., Vergnaud, J., Chaleix, V., Sol, V., Garcia, M., Gary-Bobo, M., Raehm, L. & Durand, J. O. Porphyrin-functionalized mesoporous organosilica nanoparticles for two-photon imaging of cancer cells and drug delivery. *J. Mater. Chem. B* **3**, 3681–3684 (2015).
- 203 Goyan, R. L. & Cramb, D. T. Near-infrared two-photon excitation of protoporphyrin IX: photodynamics and photoproduct generation. *Photochem. Photobiol.* **72**, 821–827 (2000).
- 204 Ogawa, K., Hasegawa, H., Inaba, Y., Kobuke, Y., Inouye, H., Kanemitsu, Y., Kohno, E., Hirano, T., Ogura, S. & Okura, I. Water-soluble bis(imidazolylporphyrin) self-assemblies with large two-photon absorption cross sections as potential agents for photodynamic therapy. *J. Med. Chem.* **49**, 2276–2283 (2006).
- 205 Collins, H. A., Khurana, M., Moriyama, E. H., Mariampillai, A., Dahlstedt, E., Balaz, M., Kuimova, M. K., Drobizhev, M., Yang, V. X. D., Phillips, D., Rebane, A., Wilson, B. C. & Anderson, H. L. Blood-vessel closure using photosensitizers engineered for two-photon excitation. *Nat. Photon.* **2**, 420–424 (2008).
- 206 Yang, P. P., Yang, Y., Gao, Y. J., Wang, Y., Zhang, J. C., Lin, Y. X., Dai, L. R., Li, J. B., Wang, L. & Wang, H. Unprecedentedly high tissue penetration capability of co-assembled nanosystems for two-photon fluorescence imaging *in vivo*. *Adv. Opt. Mater.* **3**, 646–651 (2015).
- 207 Zhao, H. X., Wang, Y. C., Zhang, L. Y. & Wang, M. One- and two-photon luminescence in graphene oxide quantum dots. *N. J. Chem.* **39**, 98–101 (2015).
- 208 Cao, L., Wang, X., Meziani, M. J., Lu, F. S., Wang, H. F., Luo, P. J. G., Lin, Y., Harruff, B. A., Veca, L. M., Murray, D., Xie, S. Y. & Sun, Y. P. Carbon dots for multiphoton bioimaging. *J. Am. Chem. Soc.* **129**, 11318–11319 (2007).
- 209 Liu, Q., Guo, B. D., Rao, Z. Y., Zhang, B. H. & Gong, J. R. Strong two-photon-induced fluorescence from photostable, biocompatible nitrogen-doped graphene quantum dots for cellular and deep-tissue imaging. *Nano Lett.* **13**, 2436–2441 (2013).
- 210 Lawrence, K., Xia, F. J., Arrowsmith, R. L., Ge, H. B., Nelson, G. W., Foord, J. S., Felipe-Sotelo, M., Evans, N. D. M., Mitchels, J. M., Flower, S. E., Botchway, S. W., Wolverson, D., Aliev, G. N., James, T. D., Pascu, S. I. & Marken, F. Hydrothermal conversion of one-photon-fluorescent poly(4-vinylpyridine) into two-photon-fluorescent carbon nanodots. *Langmuir* **30**, 11746–11752 (2014).
- 211 Tong, G. S., Wang, J. X., Wang, R. B., Guo, X. Q., He, L., Qiu, F., Wang, G., Zhu, B. S., Zhu, X. Y. & Liu, T. Amorphous carbon dots with high two-photon fluorescence for cellular imaging passivated by hyperbranched poly(amino amine). *J. Mater. Chem. B* **3**, 700–706 (2015).
- 212 Zhang, X. D., Wang, H. X., Wang, H., Zhang, Q., Xie, J. F., Tian, Y. P., Wang, J. & Xie, Y. Single-layered graphitic-C<sub>3</sub>N<sub>4</sub> quantum dots for two-photon fluorescence imaging of cellular nucleus. *Adv. Mater.* **26**, 4438–4443 (2014).
- 213 Wang, J., Zhang, Z. H., Zha, S., Zhu, Y. Y., Wu, P. Y., Ehrenberg, B. & Chen, J. Y. Carbon nanodots featuring efficient FRET for two-photon photodynamic cancer therapy with a low fs laser power density. *Biomaterials* **35**, 9372–9381 (2014).
- 214 Tang, J., Kong, B., Wu, H., Xu, M., Wang, Y. C., Wang, Y. L., Zhao, D. Y. & Zheng, G. F. Carbon nanodots featuring efficient FRET for real-time monitoring of drug delivery and two-photon imaging. *Adv. Mater.* **25**, 6569–6574 (2013).
- 215 Wang, B. B., Wang, Y. F., Wu, H., Song, X. J., Guo, X., Zhang, D. M., Ma, X. J. & Tan, M. Q. A mitochondria-targeted fluorescent probe based on TPP-conjugated carbon dots for both one- and two-photon fluorescence cell imaging. *RSC Adv.* **4**, 49960–49963 (2014).
- 216 Kozawa, D., Miyauchi, Y., Mouri, S. & Matsuda, K. Exploring the origin of blue and ultraviolet fluorescence in graphene oxide. *J. Phys. Chem. Lett.* **4**, 2035–2040 (2013).
- 217 Miao, P., Han, K., Tang, Y. G., Wang, B. D., Lin, T. & Cheng, W. B. Recent advances in carbon nanodots: synthesis, properties and biomedical applications. *Nanoscale* **7**, 1586–1595 (2015).
- 218 Choi, Y., Kim, S., Choi, M. H., Ryoo, S. R., Park, J., Min, D. H. & Kim, B. S. Highly biocompatible carbon nanodots for simultaneous bioimaging and targeted photodynamic therapy *in vitro* and *in vivo*. *Adv. Funct. Mater.* **24**, 5781–5789 (2014).
- 219 Wang, F., Dukovic, G., Brus, L. E. & Heinz, T. F. The optical resonances in carbon nanotubes arise from excitons. *Science* **308**, 838–841 (2005).
- 220 Dukovic, G., Wang, F., Song, D. H., Sfeir, M. Y., Heinz, T. F. & Brus, L. E. Structural dependence of excitonic optical transitions and band-gap energies in carbon nanotubes. *Nano Lett.* **5**, 2314–2318 (2005).
- 221 Maultzsch, J., Pomraenke, R., Reich, S., Chang, E., Prezzi, D., Ruini, A., Molinari, E., Strano, M. S., Thomsen, C. & Lienau, C. Exciton binding energies in carbon nanotubes from two-photon photoluminescence. *Phys. Rev. B* **72**, 241402 (2005).
- 222 Hui, Y. Y., Zhang, B. L., Chang, Y. C., Chang, C. C., Chang, H. C., Hsu, J. H., Chang, K. & Chang, F. H. Two-photon fluorescence correlation spectroscopy of lipid-encapsulated fluorescent nanodiamonds in living cells. *Opt. Express* **18**, 5896–5905 (2010).
- 223 Trojanek, F., Zidek, K., Dzurnak, B., Kozak, M. & Maly, P. Nonlinear optical properties of nanocrystalline diamond. *Opt. Express* **18**, 1349–1357 (2010).
- 224 Pope, I., Payne, L., Zorinants, G., Thomas, E., Williams, O., Watson, P., Langbein, W. & Borri, P. Coherent anti-Stokes Raman scattering microscopy of single nanodiamonds. *Nat. Nanotechnol.* **9**, 940–946 (2014).
- 225 Choi, J.-Y., Ramachandran, G. & Kandlikar, M. The impact of toxicity testing costs on nanomaterial regulation. *Environ. Sci. Technol.* **43**, 3030–3034 (2009).
- 226 Ye, L., Yong, K.-T., Liu, L., Roy, I., Hu, R., Zhu, J., Cai, H., Law, W.-C., Liu, J., Wang, K., Liu, J., Liu, Y., Hu, Y., Zhang, X., Swihart, M. T. & Prasad, P. N. A pilot study in non-human primates shows no adverse response to intravenous injection of quantum dots. *Nat. Nanotechnol.* **7**, 453–458 (2012).
- 227 Rivera Gil, P., Huhn, D., del Mercato, L. L., Sasse, D. & Parak, W. J. Nanopharmacy: Inorganic nanoscale devices as vectors and active compounds. *Pharmacol. Res.* **62**, 115–125 (2010).
- 228 Takahashi, H., Niidome, Y., Niidome, T., Kaneko, K., Kawasaki, H. & Yamada, S. Modification of gold nanorods using phosphatidylcholine to reduce cytotoxicity. *Langmuir* **22**, 2–5 (2006).
- 229 Kang, H., Mintri, S., Menon, A. V., Lee, H. Y., Choi, H. S. & Kim, J. Pharmacokinetics, pharmacodynamics and toxicology of theranostic nanoparticles. *Nanoscale* **7**, 18848–18862 (2015).
- 230 Kreyling, W. G., Hirn, S., Moller, W., Schlehe, C., Wenk, A., Celik, G., Lipka, J., Schaffler, M., Haberl, N., Johnston, B. D., Sperling, R., Schmid, G., Simon, U., Parak, W. J. & Semmler-Behnke, M. Air-blood barrier translocation of tracheally instilled gold nanoparticles inversely depends on particle size. *ACS Nano* **8**, 222–233 (2014).
- 231 Choi, H. S., Liu, W., Misra, P., Tanaka, E., Zimmer, J. P., Itty Ipe, B., Bawendi, M. G. & Frangioni, J. V. Renal clearance of quantum dots. *Nat. Biotechnol.* **25**, 1165–1170 (2007).



This work is licensed under a Creative Commons Attribution 4.0 International License. The images or other third party material in this article are included in the article's Creative Commons license, unless indicated otherwise in the credit line; if the material is not included under the Creative Commons license, users will need to obtain permission from the license holder to reproduce the material. To view a copy of this license, visit <http://creativecommons.org/licenses/by/4.0/>

© The Author(s) 2016